Unified Mechanics of Metallic Structural Materials

Hsiao W Lee, Drexel University, Department of Mechanical Engineering & Mechanics, Philadelphia, PA, United States
Noushad Bin Jamal, Indian Institute of Technology Department of Applied Mechanics, Madras, India
Hamidreza Fakhri, McMahon & Mann Consulting Engineering and Geology, Buffalo, NY, United States
Ravi Ranade, University at Buffalo, Civil, Structural, and Environmental Engineering, Buffalo, NY, United States
Halina Egner, Cracow University of Technology, Faculty of Mechanical Engineering, Kraków, Poland
Adam Lipski, Michał Piotrowski, and Stanisław Mroziński, Bydgoszcz University of Science and Technology, Faculty of Mechanical Engineering, Bydgoszcz, Poland
Chebolu L Rao, Indian Institute of Technology Department of Applied Mechanics, Madras, India
Milos B Djukic, University of Belgrade, Faculty of Mechanical Engineering, Belgrade, Serbia
Cemal Basaran, University at Buffalo, Civil, Structural, and Environmental Engineering, Buffalo, NY, United States

---

Abstract

Unified mechanics theory (UMT) unifies Newton's universal laws of motion and the second law of thermodynamics at the ab-initio level. As a result, governing differential equation of any structural system directly includes entropy generation in the system. The linearly independent thermodynamic state index axis (TSI) of the unified mechanics theory maps the entropy generation rate at a material point between zero and one, according to the thermodynamic fundamental equation of the material. Then, the thermodynamic lifespan of any closed system travels between zero and one along the TSI axis according to the second law of thermodynamics as formulated by Boltzmann. Because entropy generation is directly included in the differential equation of the structure, there is no need for empirical dissipation potential obtained by curve-fitting a function to dissipation/degradation test data. However, the thermodynamic fundamental

doi:10.1016/B978-0-323-90646-3.00006-X

equation of the material must be derived analytically based on fundamental principles of physics and chemistry. In this chapter, some recently developed models for metallic structural material's fatigue, corrosion, and hydrogen embrittlement behavior as well as, the temperature and strain rate-dependent flow stress modeling are presented.

Key Points

- Introduction of the unified mechanics theory.
- Modeling to predict the fatigue life of structural materials.
- Modeling corrosion and hydrogen embrittlement in structural steel.
- Modeling temperature and strain rate-dependent flow stress of steel.

Introduction to Unified Mechanics Theory

Coordinate System in Unified Mechanics Theory

Mechanics of metallic alloy structural materials have been studied extensively based on Newtonian mechanics, and various dissipation, degradation, damage evolution, and fatigue life prediction models have been proposed. However, Newtonian mechanics does not account for degradation and dissipation in the universal laws of motion. Dissipation and degradation are governed by the laws of thermodynamics. Therefore, to make laws of Newton thermodynamically consistent, traditionally, degradation and dissipation are introduced via empirical dissipation and degradation evolution functions. Because the Newtonian space-time coordinate system does not have an axis for dissipation. These empirical dissipations and degradation functions require curve fitting to test data to obtain the parameters which have no physical meaning. The dissipation constraint functions in Lagrangian mechanics are examples of empirical dissipation/degradation functions.

On the other hand, unified mechanics theory (UMT) (Basaran, 2023; Lee and Basaran, 2021) is ab-initio unification of the second law of thermodynamics and the universal laws of motion of Newton. In UMT dissipation and degradation at a material, points evolve along the thermodynamic state index axis (TSI) between coordinates of zero and one. TSI is a linearly independent fifth axis in addition to the Newtonian space-time axes. It is based on Boltzmann's formulation of the second law of thermodynamics (Boltzmann, 1877), in which entropy is stated to have a logarithmic connection with the disorder and was put into the final form by Planck (1900)

$$S = k_B \ln W \tag{1}$$

where S is the entropy, k_B is the Boltzmann constant, and W is the disorder parameter (probability of a microstate) (Boltzmann, 1877; Planck, 1900). The thermodynamic state index Φ is a unitless quantity describing the difference in disorder between the original "ordered" state (or any reference state) and the current "disordered" state,

$$s = \frac{N_A}{m_s} k_B \ln W \tag{2}$$

$$\Phi = \frac{W - W_o}{W} = \left[1 - e^{-\frac{(\Delta s)m_s}{R}}\right] \tag{3}$$

where s is the entropy per unit mass (specific entropy), N_A is Avogadro's number, m_s is the molar mass, R is the universal gas constant, Δs is the change in specific entropy at a point. In the numerical simulation of fatigue damage evolution, the thermodynamic life reaches "the end" (material fails) when TSI reaches a critical value.

$$\Phi = \left[1 - e^{-\frac{(\Delta s_{FFE})m_s}{R}}\right] = \Phi_{cr} \tag{4}$$

where Φ_{cr} is the user-defined critical value of the TSI, and Δs_{FFE} is the cumulative specific entropy at failure (also known as fatigue fracture entropy) (Naderi *et al*., 2010). It should be noted that in this chapter, if not otherwise specified, we use capital S for entropy and lower case s for specific entropy.

Based on Eq. (3), the degradation is mapped between 0, when the entropy generation rate is maximum (entropy is minimum), and near one, when the entropy generation rate is zero (entropy is maximum), along the TSI axis according to the cumulative specific entropy production rate of the system. Therefore, TSI provides a physics-based life span prediction metric for any thermodynamic process without the need for curve fitting an empirical dissipation/degradation function. However, it does require the analytically derived thermodynamic fundamental equation of the material. TSI is driven by the entropy generation equation, Δs. It should also be noted that Eq. (3) is an exponential function; it reaches the value of 1 only when the power is infinite. Therefore, a critical value of the thermodynamic state index near 1 is usually chosen, as shown in Eq. (4). However, the definition of failure is application specific. Thus, the value of Φ_{cr} needs to be defined according to the problem at hand. For example, the failure of an airplane wing cannot be defined by the airplane wing breaking into pieces in the air.

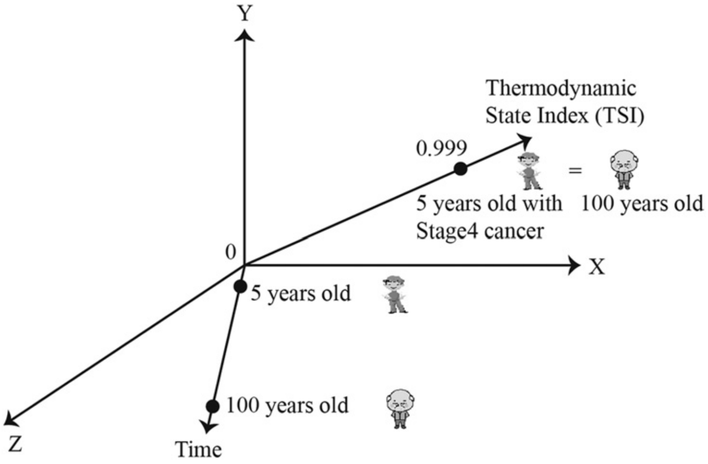

Fig. 1 Coordinate system in unified mechanics theory (UMT) (Basaran, 2023).

Fig. 1 shows the coordinate system in unified mechanics theory. It is important to emphasize that in the UMT coordinate system derivative of displacement with respect to entropy is not zero, as it is in Newtonian mechanics, because TSI is a linearly independent axis. The following example can explain the UMT coordinate system: "A 5-year-old person with a terminal illness and a 100-year-old sick person would have different coordinates in the time axis. But they have the same coordinate on the TSI axis. Because in Newtonian space-time coordinate system without a thermodynamic axis, the physical state cannot be defined. On the other hand, in the unified mechanics theory their physical state is represented by the TSI axis coordinate in addition to the space-time coordinates. On the TSI axis at $\Phi = 0.999$, a 5-year-old person with a terminal illness and a sick 100-year-old man will have the same thermodynamic state index coordinate. It is shown that they have about the same remaining life on the TSI axis. Essentially, a person's age according to the calendar does not give any information about that person's thermodynamic physical state.

Laws of Unified Mechanics Theory

Second law of unified mechanics theory

The change of momentum of a body is proportional to the impulse impressed on the body and happens along the straight line on which that impulse is impressed. Degradation of the input impulse takes place according to the second law of thermodynamics. The rate of degradation of impulse is directly proportional to the entropy generation rate in the system along the path chosen.

$$Fdt(1-\Phi) = d(mv) \tag{5}$$

Third law of unified mechanics theory

To every action, there is always opposed an equal reaction. The composition of the initial reaction of a body in response to an action will change over time as the stiffness of the reacting system degrades over time according to the second law of thermodynamics and its thermodynamic fundamental equation. The reaction will be governed by the third law of the unified mechanics theory, given by

$$F_{21} = F_{12} = \frac{dU_{21}}{du_{21}} = \frac{d}{du_{21}}\left[\frac{1}{2}k_{21}(1-\Phi)u_{21}^2\right] \tag{6}$$

Dynamic Equilibrium Equation in Unified Mechanics Theory

If there are 'n' number of different independent entropy generation mechanisms in a system, a general representation of the second law of unified mechanics theory can be given as follows,

$$Fdt(1-\Phi) = d(m\dot{u}) \tag{7}$$

Where Fdt is impulse, Φ is the thermodynamic state index which is the normalized form of the second law of thermodynamics as defined by Boltzmann, m is the mass, $\dot{u}$ is the velocity. Laws of thermodynamics govern the dissipative mechanisms, representing the energy of a system. Newton's laws of motion give the space-time coordinates of a material point.

The dynamic equilibrium equation of a dissipative system can be derived from the Lagrangian using fundamental principles of finding the local extremum of integrals.

The action of a material point, over some time, $\Delta t = t_2 - t_1$, can be defined by the following integral,

$$I = \int_{\mathrm{t}_1}^{\mathrm{t}_2} \mathscr{L} dt \tag{8}$$

where $\mathscr{L}$ represents the Lagrangian of the system (Marion, 1965). In unified mechanics theory, each material point's coordinates are defined in the space-time-TSI coordinate system (see **Fig. 1**). Hence the material point coordinates are a function of (x, y, z, t, Φ). The additional parameter Φ, called thermodynamic state index (TSI) of the material point represents the physical state of the material point. Using the unified mechanics theory, the Lagrangian of the system is written as follows,

$$\mathscr{L} = \mathscr{L}(t, u, \dot{u}, \Phi) \tag{9}$$

where t, u and $\dot{u}$ represent the time, displacement, and velocity of a material point, respectively. The term Φ represents the thermodynamic state index of a material point. If the integral function in Eq. (8) attains a local minimum at a point, q and lets $\zeta(t)$ be an arbitrary function that has at least one derivative and vanishes at the initial time, t_1 and final time, t_2; then for any real number ϵ, close to zero, the following condition is valid,

$$I(q) \leq J(\epsilon) \tag{10}$$

where the real-valued function, J is represented as follows,

$$J(\epsilon) = I(q + \epsilon\zeta) \tag{11}$$

The functional 'I' is said to have a local minimum at $u = q$, and the function J equivalently has a local minimum at $\epsilon = 0$. Hence the following equation is valid,

$$\left[\frac{dJ}{d\epsilon}\right]_{\epsilon = 0} = \int_{\mathrm{t}_1}^{\mathrm{t}_2} \left[\frac{d\mathscr{L}}{d\epsilon}\right]_{\epsilon = 0} dt = 0 \tag{12}$$

Taking the total derivative of $\mathscr{L}$, we get the following equation, which has an additional extra partial derivative term compared to the Newtonian mechanics based equilibrium equation,

$$\frac{d\mathscr{L}}{d\epsilon} = \frac{\partial\mathscr{L}}{\partial u}\frac{du}{d\epsilon} + \frac{\partial\mathscr{L}}{\partial \dot{\mathrm{u}}}\frac{d\dot{u}}{\mathrm{d}\epsilon} + \frac{\partial\mathscr{L}}{\partial\Phi}\frac{d\Phi}{d\epsilon} \tag{13}$$

It is important to point out that in Eq. (13) the derivative of Lagrangian with respect to the TSI axis is non-zero. The displacement at a point can be given by,

$$u = q + \epsilon\zeta \tag{14}$$

Taking the time derivative of Eq. (14), we obtain the velocity,

$$\dot{u} = \dot{q} + \epsilon\dot{\zeta} \tag{15}$$

Using Eq. (14) and Eq. (15), we obtain the following form of Eq. (13),

$$\frac{d\mathscr{L}}{d\epsilon} = \frac{\partial\mathscr{L}}{\partial u}\zeta + \frac{\partial\mathscr{L}}{\partial\dot{u}}\dot{\zeta} + \frac{\partial\mathscr{L}}{\partial\Phi}\frac{d\Phi}{d\epsilon} \tag{16}$$

We can write the following total derivative.
of Φ with respect to ϵ,

$$\frac{d\Phi}{d\epsilon} = \frac{\partial\Phi}{\partial u}\frac{du}{d\epsilon} + \frac{\partial\Phi}{\partial\dot{u}}\frac{d\dot{u}}{d\epsilon} \tag{17}$$

Hence, by substituting Eq. (17) in Eq. (16), we get the following equation,

$$\frac{d\mathscr{L}}{d\epsilon} = \left(\frac{\partial\mathscr{L}}{\partial u} + \frac{\partial\mathscr{L}}{\partial\Phi}\frac{\partial\Phi}{\partial u}\right)\zeta + \left(\frac{\partial\mathscr{L}}{\partial\dot{u}} + \frac{\partial\mathscr{L}}{\partial\Phi}\frac{\partial\Phi}{\partial\dot{u}}\right)\dot{\zeta} \tag{18}$$

Therefore, Eq. (12) takes the following form,

$$\int_{\mathrm{t}_1}^{\mathrm{t}_2} \left[\frac{d\mathscr{L}}{d\epsilon}\right]_{\epsilon = 0} dt = \int_{\mathrm{t}_1}^{\mathrm{t}_2} \left[\left(\frac{\partial\mathscr{L}}{\partial u} + \frac{\partial\mathscr{L}}{\partial\Phi}\frac{\partial\Phi}{\partial u}\right)\zeta\right]_{\epsilon = 0} dt + \int_{\mathrm{t}_1}^{\mathrm{t}_2} \left[\left(\frac{\partial\mathscr{L}}{\partial\dot{u}} + \frac{\partial\mathscr{L}}{\partial\Phi}\frac{\partial\Phi}{\partial\dot{u}}\right)\dot{\zeta}\right]_{\epsilon = 0} dt = 0 \tag{19}$$

Integrating the second term on the right-hand side of Eq. (19) by parts, we get the following equation,

$$\int_{t_1}^{t_2} \left[\left(\frac{\partial\mathscr{L}}{\partial u} + \frac{\partial\mathscr{L}}{\partial\Phi}\frac{\partial\Phi}{\partial u} - \frac{d}{dt}\left(\frac{\partial\mathscr{L}}{\partial\dot{u}} + \frac{\partial\mathscr{L}}{\partial\Phi}\frac{\partial\Phi}{\partial\dot{u}}\right)\right)\zeta\right]_{\epsilon = 0} dt + \left\{\left|\left[\left(\frac{\partial\mathscr{L}}{\partial\dot{u}} + \frac{\partial\mathscr{L}}{\partial\Phi}\frac{\partial\Phi}{\partial\dot{u}}\right)\zeta\right]_{\epsilon = 0}\right|\right\}_{t_1}^{t_2} = 0 \tag{20}$$

By the definition of ζ, the second term in Eq. (20) vanishes at the boundary of the integral domain. Hence, using Eqs. (14) and (15) in Eq. (20) and by applying the principle of local state, we get the following equation,

$$\frac{\partial\mathscr{L}}{\partial u} + \frac{\partial\mathscr{L}}{\partial\Phi}\frac{\partial\Phi}{\partial u} - \frac{d}{dt}\left(\frac{\partial\mathscr{L}}{\partial\dot{u}} + \frac{\partial\mathscr{L}}{\partial\Phi}\frac{\partial\Phi}{\partial\dot{u}}\right) = 0 \tag{21}$$

Unlike in the Newtonian mechanics-based Euler-Lagrange equation, Eq. (21) has an additional derivative as a function of TSI. Using Eq. (14), the variation statement of any function, Ψ in u, is represented as follows.

$$\left[\frac{d\Psi}{d\varepsilon}\right]_{\varepsilon=0} = \delta\Psi \tag{22}$$

Using Lagrange-d'Alembert's principle, and representation of variation statement, given in Eq. (22), for an externally applied force, F_{ext}, we can write the following equilibrium equation,

$$\frac{\partial\mathscr{L}}{\partial u} + \frac{\partial\mathscr{L}}{\partial\Phi}\frac{\partial\Phi}{\partial u} - \frac{d}{dt}\left(\frac{\partial\mathscr{L}}{\partial\dot{u}} + \frac{\partial\mathscr{L}}{\partial\Phi}\frac{\partial\Phi}{\partial\dot{u}}\right) + F_{ext} = 0 \tag{23}$$

Eq. (23) represents the basic form of the dynamic equilibrium equation in the unified mechanics theory. A specific form for a given system is derived by writing the thermodynamic fundamental equation of the system and the Lagrangian of the system (Bin Jamal *et al.*, 2021). Unlike in the Newtonian mechanics-based Euler-Lagrange equation, Eq. (23) has an additional derivative as a function of TSI.

Example: analysis of a single degree of freedom system

The single degree of freedom system shown in **Fig. 2** is analyzed, (Bin Jamal *et al.*, 2021), using unified mechanics, and Newtonian mechanics, and then results are compared with test data in this example. The entropy generation mechanism for the kinetic energy part and potential energy part can be evolving at different rates following the laws of thermodynamics. For this simple example, we are assuming that the only dissipation in the entire system is due to the friction between the block and the surface. All other entropy generation mechanisms are ignored for simplicity in this example. The Lagrangian of the mass-spring friction block system in the unified mechanics theory is given by the following simplified equation,

$$(1-\Phi)\mathscr{L} = \frac{1}{2}m\dot{u}^2 - \frac{1}{2}ku^2 \tag{24}$$

Where, $\dot{u}$ and u are the velocity and displacement, respectively, m is the mass of the block and k is the stiffness of the spring.

Using Eq. (23) in Eq. (24) the following force balance equilibrium equation is obtained,

$$\frac{1}{(1-\Phi)}m\ddot{u} + \frac{1}{(1-\Phi)}ku + \left(m\frac{m_s}{R}\frac{1}{(1-\Phi)}\frac{d\Delta S}{dt}\right)\dot{u} + \frac{m_s}{R}\frac{1}{(1-\Phi)}\left\{\frac{1}{2}ku^2 - \frac{1}{2}m\dot{u}^2\right\}\frac{\partial\Delta S}{\partial u} + \mathscr{g}\left(\frac{\partial\Delta S}{\partial\ddot{u}}\right) + f_{ext} = 0 \tag{25}$$

The functional, $\mathscr{g}$ is the summation of all the terms as a function of $\frac{\partial\Delta S}{\partial\ddot{u}}$. On the other hand, in Newtonian mechanics, the governing dynamic equilibrium equation for an SDOF is given by

$$m\ddot{u} + c\dot{u} + ku = f_{ext} \tag{26}$$

For SDOF sliding friction problem Eq. (26) takes the following form

$$m\ddot{u} + [\mu_f mg]\operatorname{sgn}(\dot{u}) + ku = f_{ext} \tag{27}$$

Where μ_f is the Coulomb friction coefficient, m is the mass, g is the gravitational constant, and sgn() is the signum function. The damping term c in Eq. (26) is represented by the Coulomb friction force. The Eq. (27) does not include any dissipation other than mechanical work due to friction. However, there are several entropy-generating dissipative processes, that must be accounted for in the unified mechanics dynamic equilibrium Eq. (25). These additional entropy generation mechanisms are defined in terms of change in entropy, ΔS, and can be quantified along the thermodynamic state index axis, Φ. Eqs. (25) and (27) are applied to a mass-spring single degree of freedom system shown in **Fig. 2** and the results are shown in **Fig. 3**.

In **Fig. 3** (a) results from the unified mechanics theory based model and Newtonian mechanics based model and test data are compared. It is important to point out that in the unified mechanics theory, dissipation happens along the thermodynamic state index axis. If all dissipation mechanisms are included in the thermodynamic fundamental equation the test data will be simulated exactly. However, in Newtonian mechanics, the dissipation evolution must be obtained directly from the test data we are trying to simulate. The minor difference between the test data and unified mechanics simulation is due to the approximate thermodynamic

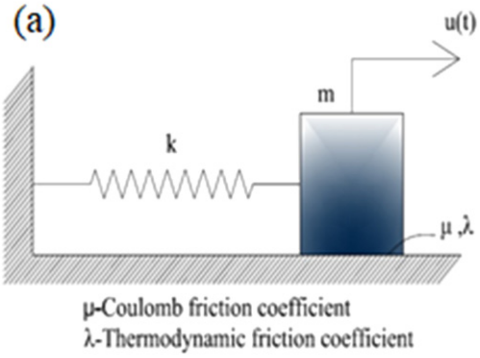

Fig. 2 SDOF mass-spring system subjected to Coulomb friction.

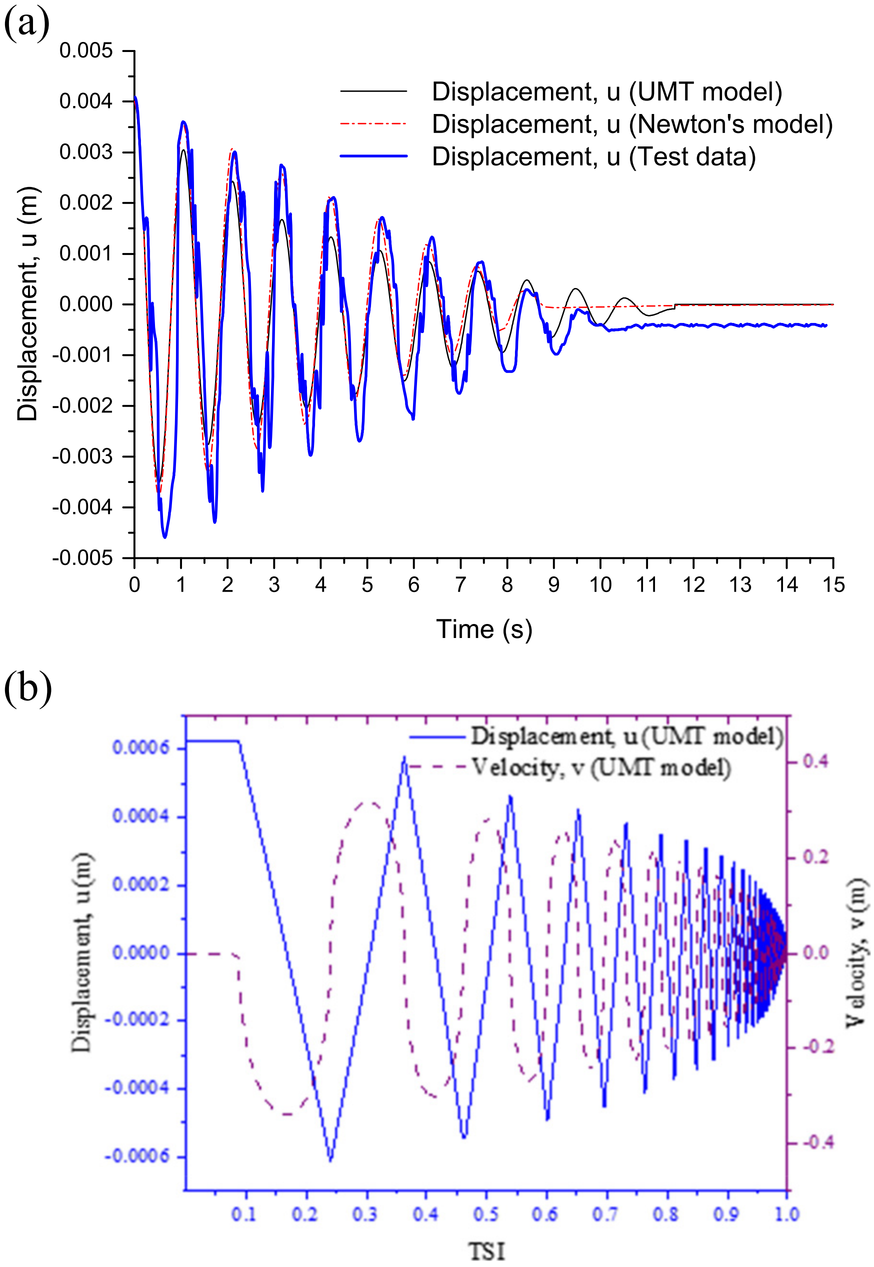

Fig. 3 (a) Comparison between model predictions and test data (Liang, 2005) for the displacement versus time data, and (b) the response along the TSI axis (Bin Jamal M *et al.*, 2021).

fundamental equation utilized. The complete description of the thermodynamic fundamental equation for this friction problem is a very challenging task and is still an active research topic.

In the following sections, some recent models, based on the UMT, related to the mechanics of metallic structural materials are presented (Lee and Basaran, 2022; Lee *et al.*, 2022a,b, 2023; Bin Jamal *et al.*, 2019, 2022).

Predicting High Cycle Fatigue Life With Unified Mechanics Theory

In this section, we discuss a model to predict the high cycle fatigue life of low-carbon steel. Compared to low cycle fatigue (LCF), which has repeated plastic deformation during the cyclic loadings, high cycle fatigue (HCF) has cyclic loading in the linear elastic range only, which results in no macro plastic deformations. Therefore, the entropy generation mechanisms that govern the thermodynamic fundamental equation of LCF and HCF are different.

During the high cycle fatigue life of low-carbon steel, six entropy generation mechanisms govern the thermodynamic fundamental equation. They are configurational entropy, ΔS_c, vibrational entropy, ΔS_{vib}, (Bin Jamal *et al.*, 2021; Lee and Basaran, 2022; Lee *et al.*, 2022a,b, 2023; Bin Jamal *et al.*, 2019, 2022; Liang, 2005; Kelly and Knowles, 2012; Reza Abbaschian and Abbaschian, 2010; Fultz, 2010) vacancy diffusion entropy, ΔS_d, (Basaran and Lin, 2008; Shidong *et al.*, 2009) heat conduction induced entropy, ΔS_t, internal (Basaran, 2023) friction (scattering) induced entropy, ΔS_r, (Basaran, 2023) and finally the microplasticity induced entropy, $\Delta S_{\mu p}$. (Lemaitre *et al.*, 1999; Doudard *et al.*, 2005; Charkaluk and Constantinescu, 2009; Fan *et al.*, 2018) Because entropy is an additive property, we can write the thermodynamic fundamental equation for the total entropy production as follows (Lee and Basaran, 2022)

$$\Delta S = \Delta S_c + \Delta S_{vib} + \Delta S_d + \Delta S_t + \Delta S_r + \Delta S_{mp} \tag{28}$$

In the derivation of the thermodynamic fundamental equation, the following assumptions were made:

1. Applied maximum stress is below the yield stress of the material, hence no global macroscopic plastic deformation occurs.
2. Point defects such as vacancies, interstitials, and impurities, can be built-in with the original crystal growth or created by energy input during the fatigue process.
3. Input mechanical energy increases vacancies and dislocation densities. However, the increasing dislocation density only causes hardening at the micro-level and never induces macroscopic plastic deformation as the maximum applied mean stress is below the yield stress. The vacancy generation/diffusion and dislocation motions (e.g., cross slip) around inclusions induce irreversibility at a micro-level under elastic cyclic loads (Lemaitre *et al.*, 1999; Doudard *et al.*, 2005; Charkaluk and Constantinescu, 2009; Fan *et al.*, 2018; Callister and Rethwisch, 2020; Marti *et al.*, 2020a; Mughrabi, 2013; Ho *et al.*, 2017; Mughrabi, 2009).
4. A mechanism called micro-plasticity (Lemaitre *et al.*, 1999; Doudard *et al.*, 2005; Charkaluk and Constantinescu, 2009; Fan *et al.*, 2018) is expected to happen at some micro defects sites such as vacancies, dislocations, and hydrogen solute atoms at the micro-level due to stress localization.
5. During fatigue loading, the vacancy concentration gradient in the sample results in vacancy diffusion, and the temperature gradient in the sample results in thermomigration.
6. Temperature evolution in the sample during fatigue loading is determined by microplastic work, internal friction (scattering), heat conduction, and thermoelastic damping.

Configurational Entropy Production

The rearrangement and redistribution of atoms in the metal crystal lattice due to input mechanical energy during the elastic cycling loading result in entropy production (Bin Jamal *et al.*, 2021; Reza Abbaschian and Abbaschian, 2010). The configurational entropy S_c is a concept from statistical thermodynamics that uses the binomial distribution formula $P = \frac{N!}{(N-n)!n!}$ to replace the disorder parameter W in Eq. (1), which is written in the following form (Boltzmann, 1877; Planck, 1900; Bin Jamal *et al.*, 2021; Reza Abbaschian and Abbaschian, 2010):

$$S_c = k_B \ln\left(\frac{N!}{(N - n_{vac})!n_{vac}!}\right) \tag{29}$$

where N is the number of lattice sites and n_{vac} is the number of atomic vacancies.

Atomic vacancies and defects result from missing atoms from their original lattice sites, which are rearranged due to the thermally activated transport. The entropy production due to the variation of configurational entropy ΔS_c from temperature T_1 to T_2 is given by,

$$\Delta S_c = k_B\left[\ln\left(\frac{N!}{(N - n_{vac2})!n_{vac2}!}\right) - \ln\left(\frac{N!}{(N - n_{vac1})!n_{vac1}!}\right)\right] \tag{30}$$

where n_{vac1} and n_{vac2} are the number of vacancies at T_1 and T_2, respectively.

The thermodynamic equilibrium vacancy concentration C_v required for computing the number of vacancies n_{vac} in Eq. (30) can be calculated by

$$C_v = \frac{n_{vac}}{N} = \exp\left(\frac{T\Delta S_v - \Delta h_f}{k_B T}\right) \tag{31}$$

where n_{vac} is the number of vacancies, Δh_f is the vacancy formation enthalpy which is indistinguishable from the vacancy formation energy ΔE_f if the volume is kept constant. The vacancy formation energies ΔE_f for different metals are readily available in the literature, such as (Burton, 1972; Mattsson and Mattsson, 2002).

Vibrational Entropy Production

The vibrational entropy is also a concept from statistical thermodynamics (or physical chemistry) that replaces disorder parameter W with the phase state of the atoms as they vibrate, which is defined by the momentum and position coordinates (Fultz, 2010; Atkins *et al.*, 2018; Cahn and Haasen, 1996; Laughlin and Hono, 2014). The vibrational state of the atoms changes when vacancies are created. There are various molecular dynamics simulation models to precisely calculate vibrational entropies when a certain number of vacancies are removed. It is assumed the variation of vibrational entropy is the same when each atomic vacancy is created (Burton, 1972). Therefore, the total vibrational entropy production in the system is given by

$$\Delta S_{vib} = (n_{vac2} - n_{vac1})\Delta S_v \tag{32}$$

In which n_{vac1} and n_{vac2} are the number of vacancies at the temperatures T_1 and T_2, respectively. ΔS_v is the change in vibrational entropy when one atomic vacancy is created.

Entropy Generation due to Vacancy Concentration Gradient-driven Diffusion

During the fatigue process concentration of vacancies in the metal is not uniform. As a result, there is a vacancy concentration gradient, which is the driving force behind diffusion, (Basaran, 2023; Basaran and Lin, 2008; Shidong *et al.*, 2009; Teng *et al.*, 2020; Basaran *et al.*, 2003; Basaran and Lin, 2007; Yao and Basaran, 2013a,b,c). The concentration of atomic vacancies should be higher around the circumference and lower at the center for specimens with a round cross-section (for high cycle fatigue, cracks usually initiate from the surface), hence causing vacancy diffusion.

The entropy generation due to vacancy flux caused by thermo-migration (atoms migrate from the hot region to cold leaving behind vacancies), and vacancy concentration gradient, ΔS_d, is extensively studied, (Basaran, 2023; Basaran and Lin, 2008; Shidong *et al.*, 2009; Basaran *et al.*, 2003; Basaran and Lin, 2007; Yao and Basaran, 2013a,b,c). It is given by the following relation.

$$\Delta S_d = \int_{t_0}^{t} \left[\frac{C_v D_v}{k_B T^2} \left(\frac{Q^* \nabla \mathrm{T}}{T} + \frac{k_B T}{c} \nabla c \right)^2 \right] dt \tag{33}$$

where k_B is the Boltzmann constant, c is normalized vacancy concentration; $c = C_v / C_{v_0}$ in which C_{v_0} is the thermodynamic equilibrium vacancy concentration in the absence of a stress field, C_v is instantaneous atomic vacancy concentration. D_v is effective vacancy diffusivity, T is absolute temperature, Q^* is the heat of transport, which is the isothermal heat transmitted by the moving atom in the process of jumping a lattice site.

Entropy Generation due to Thermal Conduction

During high cycle fatigue, the surface temperature evolution of the sample due to thermal mechanical coupling results in a temperature gradient. The irreversible heat flow due to the temperature gradient causes entropy generation. The entropy generation equation is given by Basaran (2023); Basaran and Lin (2008); Shidong *et al.* (2009); Teng *et al.* (2020); Basaran *et al.* (2003); Basaran and Lin (2007); Yao and Basaran (2013a,b,c),

$$\Delta S_t = -\int_{t_0}^{t} \left(k_h \frac{\nabla T \cdot \nabla T}{T^2} \right) dt \tag{34}$$

where k_h is the coefficient of heat conduction, and ∇T is the temperature gradient. Eq. (34) is essentially the product of temperature gradient (thermodynamic force) ∇T and heat flux $\mathrm{J}_q = -k_h \nabla T$.

Entropy Generation due to Internal Friction (Scattering)

The entropy generation due to internal friction (phonon scattering or self-heating) is given by, (Basaran, 2023; Basaran and Nie, 2004)

$$\Delta S_r = \int_{t_0}^{t} \frac{\rho r}{T} dt \tag{35}$$

From a microscopic perspective, the temperature is defined by the intensity of atomic vibrations. The heat generation per unit mass due to internal friction, r, is due to the increasing intensity of atomic vibrations in the crystal from micro-mechanisms such as the breaking of atomic bonds, fast-moving dislocation, and phonon-phonon scattering, phonon-electron-scattering, electron scattering (called internal friction) (Huang *et al.*, 2008a; De Hosson *et al.*, 2001; Fan *et al.*, 2021). This term is different than the heat generated through the macroscopic observable plastic work or thermoelastic source.

Through the molecular dynamics simulation study (Lee and Basaran, 2022), it is shown that the lattice-stretching and atomic bond breaking does not contribute to entropy production, significantly. As for the dislocation and phonon-dragging mechanisms, they will be discussed in Section "Modeling Ultrasonic Vibration Fatigue" because they are only activated at high strain rates. In this model, the focus is the low strain rate behavior of materials.

Entropy Generation due to Microplasticity

The term micro-plasticity is used in two-scale models, which were initially developed by Lemaitre *et al.* (1999) and then reformulated by Doudard *et al.* (2005). The fatigue regime in the material is investigated based on an RVE (representative volume element) and divided into two parts: elastic matrix part and elastic-plastic inclusion part. From the macroscopic view, the material is deformed elastically during the elastic cyclic loading while from the microscopic view microplasticity is activated due to high-stress concentration at defects and localized dislocation slip planes (Lemaitre *et al.*, 1999; Doudard *et al.*, 2005; Charkaluk and

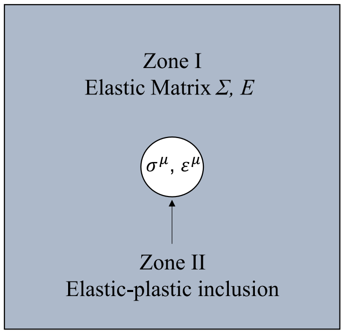

Fig. 4 A representative volume element of the two-scale model.

Constantinescu, 2009; Fan *et al.*, 2018), as shown in **Fig. 4**, schematically. The law of localization and homogenization is applied to deduce the relationship between macroscopic stress tensors and the microscopic stress and microscopic plastic strain tensors (Lemaitre *et al.*, 1999; Doudard *et al.*, 2005; Fan *et al.*, 2018).

Microscopic stress tensor is given by Charkaluk and Constantinescu (2009),

$$\sigma^{\mu} = \Sigma - 2\mu(1-b)(1-f_v)\varepsilon_p^{\mu} \tag{36}$$

where σ^{μ} is microscopic stress tensor, Σ is macroscopic stress tensor, μ is the Lame's constant, b is a material constant related to μ and bulk modulus, K, f_v is the volume fraction of lattice defects experiencing microplasticity, E is a macro strain tensor, and ε_p^{μ} is a microscopic plastic strain tensor. If the material experiences the same elastic behavior at the mesoscopic and the macroscopic scale, the previous relation implies,

$$\varepsilon_e^{\mu} = E - [(1-b)(1-f_v)]\varepsilon_p^{\mu} \tag{37}$$

where ε_e^{μ} is the microscopic elastic strain tensor.

A computational scheme for the microplastic strain increment was proposed by Charkaluk and Constantinescu (2009), as follows

$$\Delta\varepsilon_p^{\mu} = \frac{\sqrt{\frac{3}{2}}\|A_{n+1}^{*}\| - \sigma_{y0}^{\mu}}{\sqrt{\frac{3}{2}}\left(2\mu(1-b)(1-f_v) + \frac{2}{3}\mathrm{h}\right)} \frac{A_{n+1}^{*}}{\|A_{n+1}^{*}\|} \tag{38}$$

In which h is the hardening modulus, and A_{n+1}^{*} isgiven by,

$$A_{n+1}^{*} = \mathrm{dev}(\Sigma_n) - \left(2\mu(1-b)(1-f_v) + \frac{2}{3}\mathrm{h}\right)\varepsilon_{p,n}^{\mu} + \mathrm{dev}(\Delta\Sigma) \tag{39}$$

For the microplasticity model, linear kinematic hardening is utilized as a first approximation. The yield criterion is given by,

$$f = \sqrt{(S^{\mu} - \alpha^{\mu d}) : (S^{\mu} - \alpha^{\mu d})} - \sqrt{2/3}\sigma_{y0}^{\mu} = 0 \tag{40}$$

and the hardening rule is given by

$$\dot{\alpha}^{\mu} = h\dot{e}^{\mu p}\frac{1}{\sigma_{y0}^{\mu}}(\sigma^{\mu} - \alpha^{\mu}) = h\sqrt{2/3\dot{\varepsilon}_{ij}^{\mu p} \quad \dot{\varepsilon}_{ij}^{\mu p}}\,\frac{1}{\sigma_{y0}^{\mu}}(\sigma^{\mu} - \alpha^{\mu}) \tag{41}$$

where S^{μ} is the microscopic deviatoric stress, $\alpha^{\mu d}$ is the deviatoric part of the microscopic back stress, $e^{\mu p}$ is the microscopic equivalent plastic strain, σ_{y0}^{μ} is the microscopic initial yield stress, $(\sigma^{\mu} - \alpha^{\mu})$ is the kinematic translation of the microscopic yield surface under Ziegler's kinematic hardening rule, h is the kinematic linear hardening modulus defined as the slope of the stress-strain curve for a finite plastic strain value, $h = (\sigma^{\mu} - \sigma_{y0}^{\mu})/\varepsilon^{\mu p}$.

Therefore, the entropy generation due to microplasticity is given by

$$\Delta S_{mp} = \int_{t_0}^{t} \Phi f_v \frac{\sigma^{\mu} : \dot{\varepsilon}_p^{\mu}}{T} dt \tag{42}$$

During the microscopic plastic deformation, some plastic work is stored as dislocation stored energy. This stored dislocation energy is accounted for in the hardening of the material, which is included in Eq. (41). The reason to incorporate the TSI value Φ into microplastic work is to account for the increased probability of micro defects that are created in the specimen during the fatigue process.

In Eqs. (36–39), (42), f_v is the ratio of the activated volume of the micro-defects in the region V_D to the elastic matrix V_{matrix} (Charkaluk and Constantinescu, 2009; Cugy and Galtier, 2002). f_v is also defined as the maximum percentage of dislocation planes that can be activated. Assuming (Doudard *et al.*, 2005; Charkaluk and Constantinescu, 2009; Cugy and Galtier, 2002) that the percentage of the active slip bands' area in the center of the gauge section is close to the volume fraction of defects (dislocations) in the matrix, then this value can be determined by scanning electron microscopy (SEM).

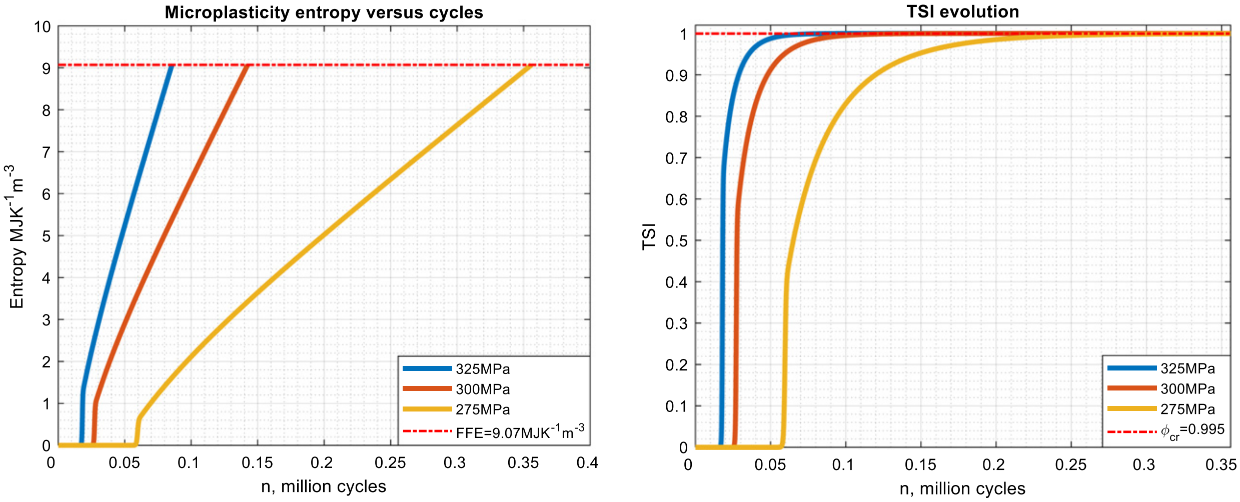

Fig. 5 (a) Accumulated total entropy production versus the number of cycles for various mean stress amplitudes (b) TSI evolution versus the number of cycles for various mean stress amplitudes.

Fatigue Life Estimation for Conventional High Cycle Fatigue

Conventional high-cycle fatigue implies that the loading frequency is less than 100 Hz. From the numerical study and order of magnitude comparison given in Lee and Basaran (2022), for conventional high cycle fatigue entropy generation due to microplasticity is at least two orders of magnitude bigger than other mechanisms. Hence, from Eqs. (3) and (42) we conclude that the TSI equation for this HCF problem can be given by

$$\Phi = 1 - \exp\left(-\frac{m_s}{R} \int_{t_0}^{t} \Phi f_v \frac{\sigma^{\mu} : \dot{\varepsilon}_P^{\mu}}{\rho T} dt \right) \tag{43}$$

Eq. (43) is exponential; hence, it never reaches unity. In practice, we determine a critical value Φ_{cr} as a threshold. We consider the specimen is failed when Φ reaches $\Phi_{cr} = 0.995$, since the probability of reaching maximum entropy at this state is 99.5 %. **Fig. 5** (a) shows the microplasticity entropy production, and (b) shows the TSI evolution, for 3 different mean stress amplitudes in DP600 steel. In **Fig. 5** maximum entropy value reached failure is independent of the cycling mean stress applied during fatigue loading. This maximum entropy is usually referred to as fatigue fracture entropy, (Naderi *et al.*, 2010).

Fig. 6 shows the stress versus the number of cycles to failure (S-N) curves based on simulations and experimental data.

Modeling Ultrasonic Vibration Fatigue

Typically, there are two types of high-cycle fatigue testing. One is the conventional high-cycle fatigue testing performed using a servo-hydraulic machine with a cycling frequency below 100 Hz. The other is the ultrasonic vibration fatigue testing conducted under an ultrasonic vibration machine that generates harmonic sinusoidal longitudinal vibrations with a frequency of 20–30 kHz in the axial direction of the sample. The degradation and failure mechanisms in ultrasonic vibration fatigue are different from the conventional high cycle fatigue due to the high strain rate loading that leads to phonon scattering and rapid temperature rise in the material (Lee *et al.*, 2022a).

The high cycle fatigue (HCF) model presented in the previous section can not predict the ultrasonic vibration fatigue life of the test sample. It is shown in the previous section that there are more than half a dozen entropy generation mechanisms during the high-cycle fatigue process. It is verified that mechanisms such as vacancy configuration, vacancy formation, and vacancy diffusion are negligible compared to other entropy generation mechanisms (Lee *et al.*, 2022a). Therefore, this model focuses only on the 3 mechanisms that govern entropy generation during ultrasonic vibration fatigue. The thermodynamic fundamental equation for the total entropy production during the ultrasonic vibration fatigue can be written as follows

$$\Delta S = \Delta S_t + \Delta S_r + \Delta S_{mp} \tag{44}$$

Where ΔS_t is entropy generation due to thermal conduction, ΔS_r is entropy generation due to internal friction (scattering), and ΔS_{mp} is the entropy generation due to microplastic work.

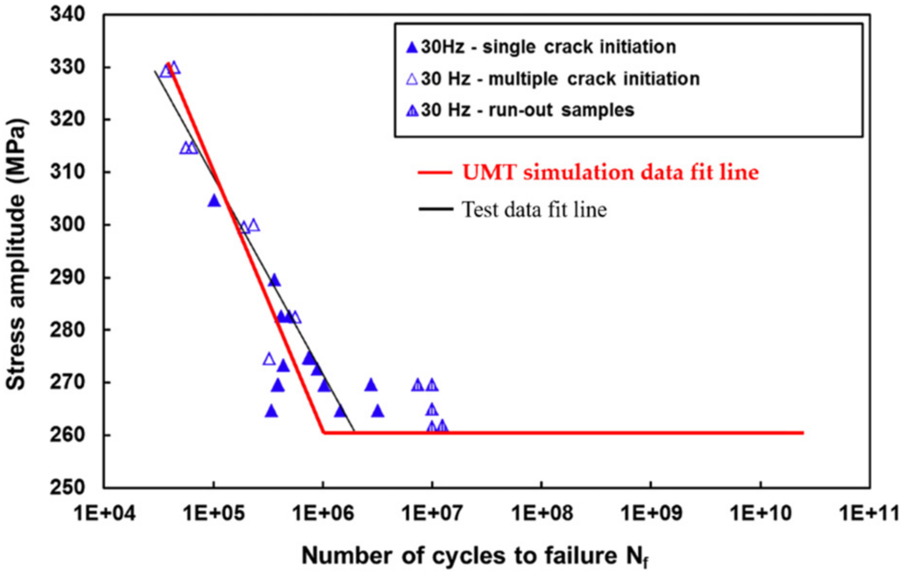

Fig. 6 Comparison of fatigue data and model predictions for tension-compression fatigue tests on dual-phase DP600 steel without any pre-strain. (The experimental S-N curve is obtained from Torabian *et al.* (2017)).

Entropy Generation due to Thermal Conduction in Ultrasonic Vibration Fatigue

The temperature gradient in the sample causes an irreversible heat flow during fatigue loading, leading to entropy generation, see Eq. (34). This term becomes non-negligible in ultrasonic vibration fatigue because the temperature rises rapidly even if the sample is subjected to ambient temperature forced-air cooling, compared to conventional HCF where the temperature change in the sample is negligible. **Fig. 7** shows the surface temperature distribution in the sample, where it is observed that the temperature in the middle of the sample reaches 150 °C near the end of the test (start of macro cracking).

Entropy Generation due to Internal Friction in Ultrasonic Vibration Fatigue

The heat generation per unit mass due to internal friction, r, mentioned in Section "Predicting High Cycle Fatigue Life with Unified Mechanics Theory" can be derived analytically. It has been shown in the literature (Huang *et al.*, 2008a; De Hosson *et al.*, 2001; Fan *et al.*, 2021; Blaschke, 2019; Blaschke *et al.*, 2019; Galligan *et al.*, 2000; Parvin and Kazeminezhad, 2016) that the rate of internal heat generation is composed of two mechanisms: (1) the drag (friction due to scattering) process involves phonon drag, electron drag, and radiation drag (De Hosson *et al.*, 2001; Blaschke, 2019; Galligan *et al.*, 2000), and (2) the dislocation motion during the plastic deformation (Huang *et al.*, 2008a; Parvin and Kazeminezhad, 2016). The internal heat generation equation for these two mechanisms is given by

$$\rho r^{drag} = \varrho B^{drag} v \ v \tag{45}$$

$$\rho r^{dis} = \frac{1}{2}\mu b^2 \dot{\varrho} - \alpha_H \mu b \sqrt{\varrho}\dot{\gamma} \tag{46}$$

where ρ is the mass density, B^{drag} and v represent the effective drag coefficient and velocity of dislocation, respectively. The terms μ, b, ϱ, and α_H are the shear modulus, the magnitude of Burger's vector, total dislocation density, and Taylor's hardening parameter, respectively. In Eq. (45), the velocity of dislocation is related to the applied shear strain rate, $\dot{\gamma}$ as follows,

$$v = \frac{\dot{\gamma}}{\varrho_m b} \tag{47}$$

where ϱ_m is the density of mobile dislocations. Hence, the entropy change due to internal friction can be given by

$$\Delta S_r = \int_{t_0}^{t} \frac{\rho r}{T} dt = \int_{t_0}^{t} \frac{\left(\varrho B^{drag} v \ v + \frac{1}{2}\mu b^2 \dot{\varrho} - \alpha_H \mu b \sqrt{\varrho}\dot{\gamma}\right)}{T} dt \tag{48}$$

Entropy Generation due to Microplasticity in Ultrasonic Vibration Fatigue

The microplasticity entropy generation can be given by the following equation:

$$\Delta S_{mp} = \int_{t_0}^{t} \Psi_f \left(\Phi f_v \frac{\sigma^\mu : \dot{\varepsilon}_P^\mu}{T}\right) dt \tag{49}$$

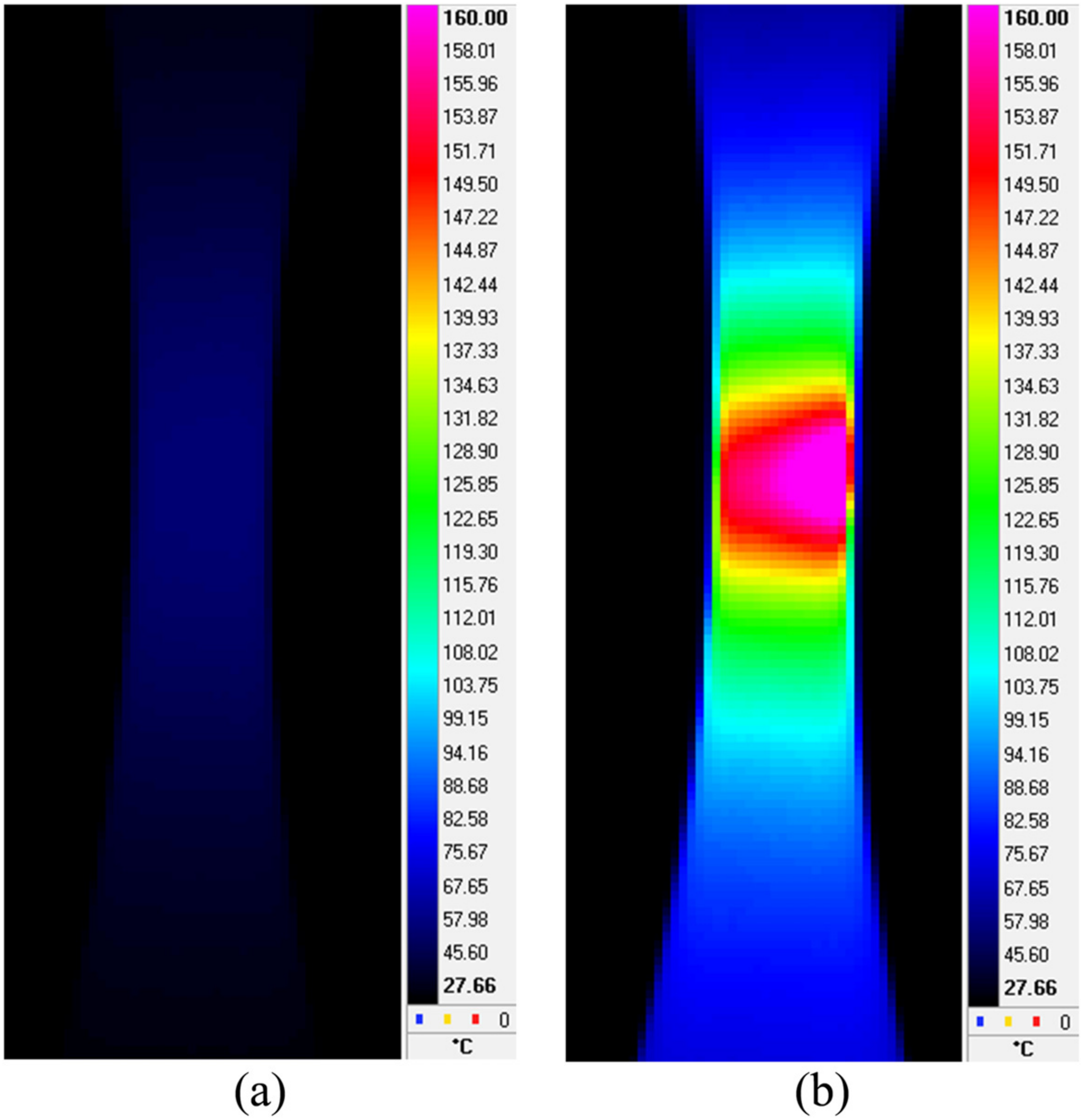

Fig. 7 Temperature distribution on the surface of the specimen at a) Start of the test; b) Near the end of the test (start of cracking). For the mean stress amplitude of $\sigma = 400$ MPa.

$$\Psi_f = \begin{cases} 1, & \text{if } f_p < 100\text{Hz (typical servo} - \text{hydraulic machine)} \\ \dfrac{100}{f_p}, & \text{if } f_p \text{ is in the order of kHz (ultrasonic vibration)or less} \end{cases} \tag{50}$$

where Ψ_f is a frequency coefficient, used to relate the loading frequency, f_p, with entropy generation rate. As the frequency of cycling loading increases microplasticity and its entropy generation decrease. The entropy source from this frequency effect can be attributed to the time-dependent screw dislocation cross-slip involved in the persistent slip band (PSB) formation, which results in microplasticity. Eq. (50) is based on the cross-slip probability, which assumes that the time duration to activate dislocation cross-slip is inversely related to the loading frequency. The cross-slip probability P is given by (Marti *et al.*, 2020b),

$$P = \beta \frac{l}{l_0} \frac{\delta t}{t_0} \exp\left(\frac{\tau_{css} - \tau_{csR}}{k_B T} V\right) \tag{51}$$

where β is a normalization coefficient ensuring that $0 < P < 1$, l/l_0 is the ratio of the length of a screw dislocation segment to a reference length $l_0 = 1$ mm, $\delta t/t_0$ is the ratio of the considered time to a reference time, V is the activation volume associated with cross slip, $(\tau_{css} - \tau_{csR})$ compares the resolved shear stress τ_{css} on the cross-slip system to a threshold critical shear stress τ_{csR} required to activate cross slip, k_B is Boltzmann's constant, and T is the absolute temperature.

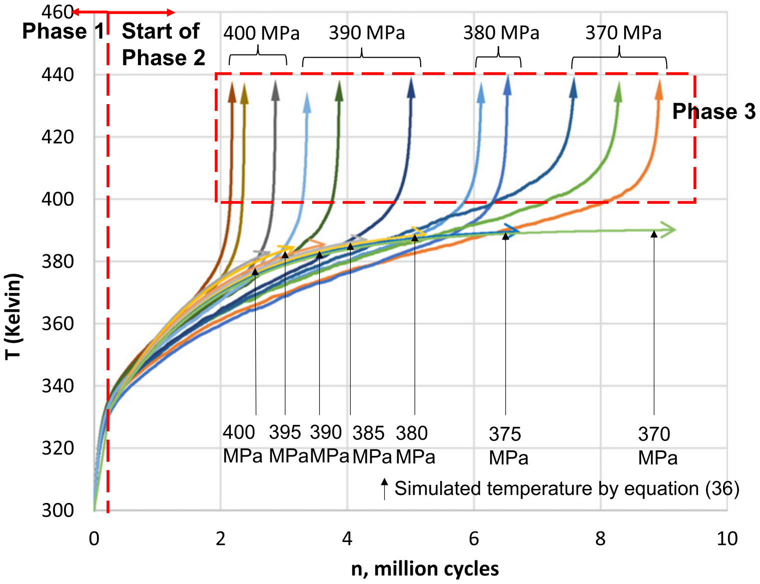

Fig. 8 Surface temperature evolution at the gage center during ultrasonic vibration versus the number of cycles under various stress amplitudes based on Eq. (53), compared with test data.

It should be noted that Eq. (50) only applies to fatigue problems where slip band formation dominates the crack initiation process (surface initiation). If the mean stress level is below the fatigue limit, microplasticity becomes negligibly small, hence, it can be ignored.

Fatigue Life Estimation for Ultrasonic Vibration Fatigue

Finally, the thermodynamic state index for ultrasonic vibration fatigue can be written as

$$\Phi = 1 - \exp\left[-m_s\left(\int_{t_0}^{t}\Psi_f\left(\Phi f_v\frac{\sigma^{\mu} : \dot{\varepsilon}_P^{\mu}}{\rho T}\right)dt + \int_{t_0}^{t}\frac{\left(\varrho B^{drag}v\, v + \frac{1}{2}\mu b^2\dot{\varrho} - \alpha_H\mu b\sqrt{\varrho}\dot{\gamma}\right)}{\rho T}dt - \int_{t_0}^{t}\left(k_h\frac{\nabla T\cdot\nabla T}{\rho T^2}\right)dt\right)\right] \tag{52}$$

In Eq. (52), the temperature cannot be assumed as constant because the high strain rate in ultrasonic vibration fatigue loading induces high temperature in the material. The temperature evolution at a material point can be derived from the classical thermal-mechanical coupling equation (Basaran, 2023; Basaran and Nie, 2004), as shown in Eq. (53),

$$\Delta T_{n+1} = -\ell_{eq}(T_n - T_0) + \frac{\Psi_f}{\rho c_V}\left[\Phi f_v\left({\sigma^{\mu}}_{n+1}\bar{\varepsilon}_P^{\mu}\right)\right]\Delta t + \frac{1}{\rho c_V}\varrho B^{drag}\left(\frac{\dot{\gamma}_{n+1}^{\mu}}{\varrho_m b}\right)^2\Delta t + \frac{1}{\rho c_V}\frac{1}{2}\mu b^2\Delta\varrho_{n+1} - \frac{1}{\rho c_V}\frac{1}{2}\alpha_H\mu b\sqrt{\varrho}\dot{\gamma}_p^{\mu}\Delta t. \tag{53}$$

where c_V is specific heat capacity, $\ell_{eq} = \Delta t/\tau_{eq}$ and $\rho c_V\frac{\theta}{\tau_{eq}} \cong -k_h\nabla^2 T$ is responsible for the thermal conduction in the material. **Fig. 8** shows the temperature evolution on the surface of the gauge center of the sample, for the test data and simulation. **Fig. 9** (a) shows the total entropy production for different mean stress amplitudes. All mean stress levels reach the same total entropy value at failure. This critical entropy value is called fatigue fracture entropy (FFE) (Naderi *et al.*, 2010). **Fig. 9** (b) shows the TSI evolution, for different fatigue mean stress amplitudes. **Fig. 10** shows the comparison between the simulated S-N curve and the experimental data.

Stress versus the number of cycles data from the experiments is scattered in a band. Unified mechanics theory prediction is in the middle of this band. Because Boltzmann has shown that the disorder will evolve following an exponential function, however, individual states will be scattered around this function. We can explain this with the following example, if we flip a coin an infinite number of times it will have a 50 % possibility of a head and a 50 % possibility of a tail. However, the first 5 times can be all head. But the equilibrium average will be a 50 % chance of being head, see **Fig. 11**.

Modeling Fatigue of Pre-Corroded Body-Centered Cubic Metals With Unified Mechanics Theory

Corrosion of steel in the presence of sodium chloride (NaCl) is a common degradation problem in reinforced concrete structures due to the inherent porosity of concrete. Using UMT, this section presents a model to estimate the ultrasonic vibration fatigue life of pre-corroded low-carbon steel that has a bcc lattice structure. To validate the model, a series of corrosion tests were performed on A656-grade steel samples in 5 wt% NaCl aqueous solution at a pH level of 7. The corrosion measurements were made with a potentiostat. Then, a series of fatigue tests were conducted on these corroded samples at a cycling frequency of 20 kHz.

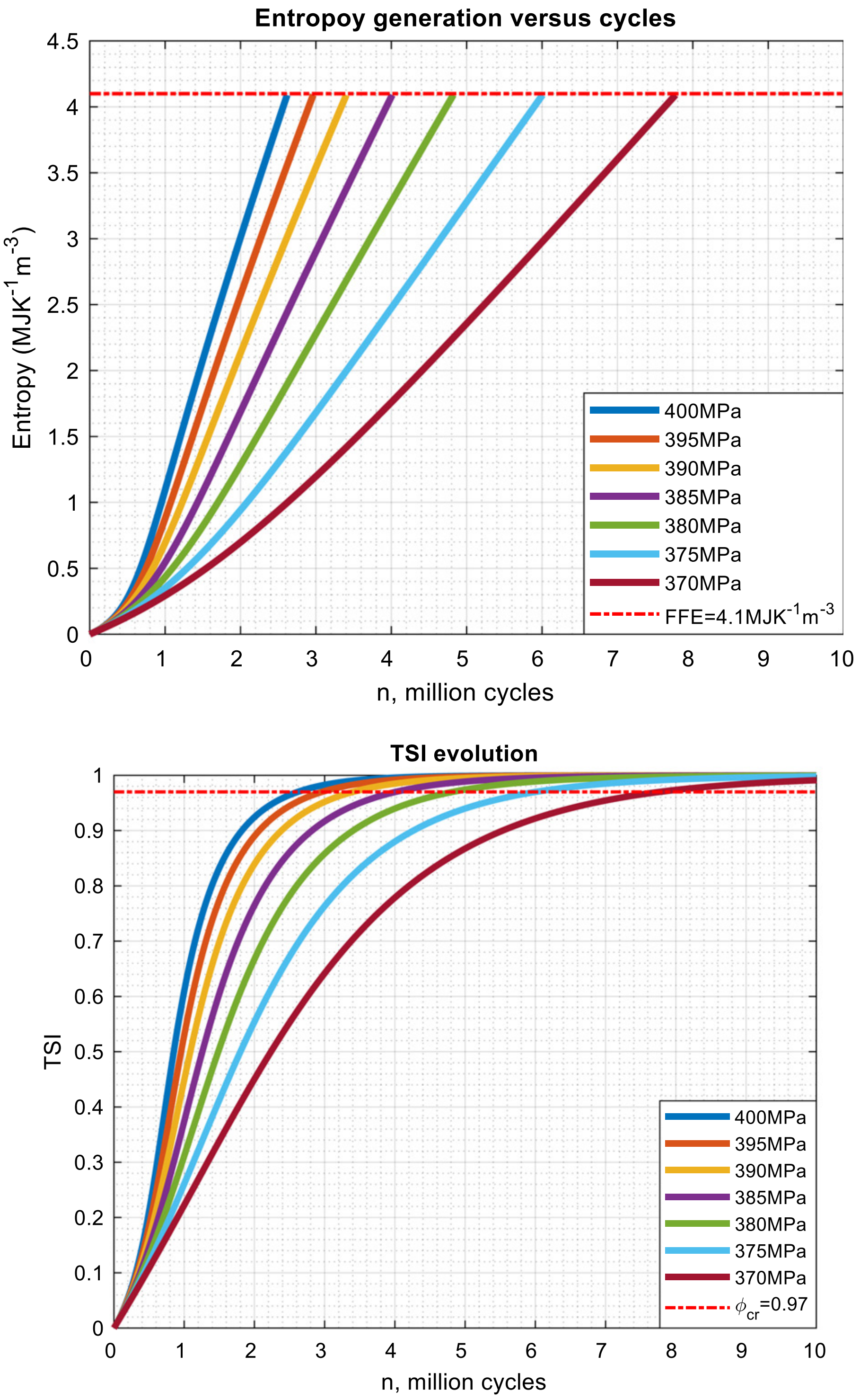

Fig. 9 (a) Accumulated total entropy production versus the number of cycles for various mean stress amplitudes (b) TSI evolution versus the number of cycles for various mean stress amplitudes.

The thermodynamic fundamental equation for pre-corroded steel subjected to ultrasonic vibration is given by,

$$\Delta S = \Delta S_{corr} + \Delta S_{mec} \tag{54}$$

where ΔS is the total entropy generation, ΔS_{corr} is the entropy generation due to corrosion, and ΔS_{mec} is the entropy generation due to mechanical loading, discussed thoroughly in Sections "Predicting High Cycle Fatigue Life with Unified Mechanics Theory" and "Modeling Ultrasonic Vibration Fatigue". The corrosion entropy production can be further divided into four mechanisms,

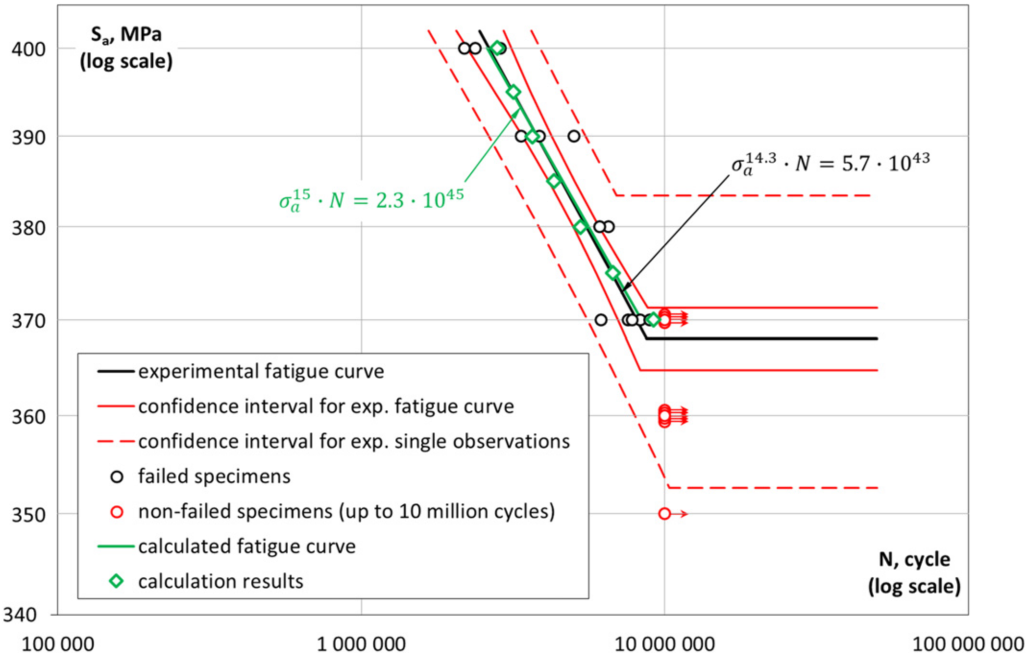

Fig. 10 Comparison between the model and the experimental fatigue data (Lee *et al.*, 2022a,b).

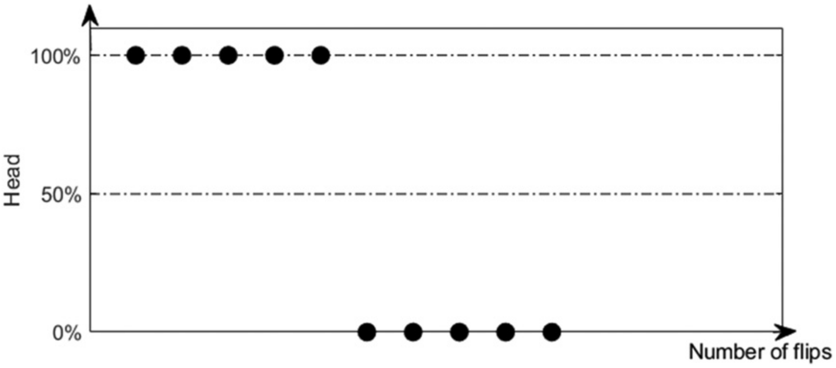

Fig. 11 Probabilistic distribution.

$$\Delta S_{corr} = \Delta S_{act} + \Delta S_{react} + \Delta S_{conc} + \Delta S_{\Omega} \tag{55}$$

Where ΔS_{act} is the entropy generation due to electrochemical overpotential, ΔS_{react} is the entropy generation due to reaction overpotential, ΔS_{conc} is the entropy generation due to diffusion overpotential, and ΔS_{Ω} is the entropy generation due to ohmic loss. In this section, the focus is only on the first two entropy generation mechanisms (ΔS_{act} and ΔS_{react}) because the latter two are negligible when the NaCl solution is well mixed there is a very low chemical concentration gradient and when the electrolyte has a strong conductivity, respectively (Imanian and Modarres, 2015).

Entropy Generation due to Electrochemical Activation Overpotential

The entropy generation equation for metal corrosion has been extensively studied based on the theory of chemical kinetics and fundamentals of irreversible thermodynamics. The entropy generation during the corrosion process is computed using the multiplication of thermodynamic forces (chemical affinity) and fluxes (corrosion current densities).

For a redox reaction, it is

$$\begin{aligned} M &\leftrightarrow M^{z^+} + ze^- \\ O + ze^- &\leftrightarrow R \end{aligned} \tag{56}$$

where M represents the species being oxidized, O represents the species being reduced, z is the number of valence electrons involved in the reaction. Imanian and Modarres (2015), extended the work of Gutman (1998) and Lu and Luo (2006), to formulate entropy generation in corrosion in a more comprehensive formulation

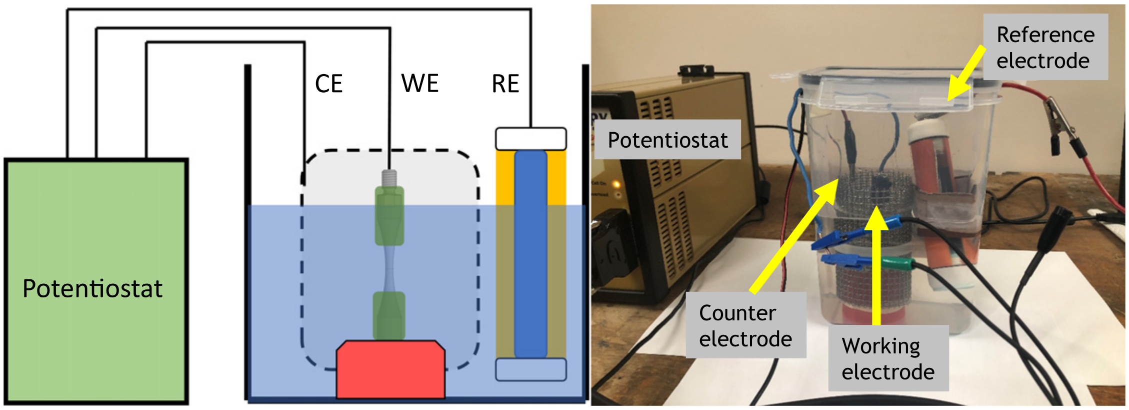

(a) (b)

Fig. 12 (a) Schematic illustration of the electrochemical cell; (b) photograph of the electrochemical cell.

$$\Delta S_{act} = \frac{1}{T}\int_{t_0}^{t} \left[J_{M,a}\alpha_M\tilde{A}_M + J_{M,c}(1-\alpha_M)\tilde{A}_M + J_{O,a}\alpha_O\tilde{A}_O + J_{O,c}(1-\alpha_O)\tilde{A}_O\right]dt_{corr} \tag{57}$$

where $J_{M,a}$ and $J_{M,c}$ are the irreversible anodic and cathodic activation fluxes (thermodynamic fluxes) for oxidation reaction, $J_{O,a}$ and $J_{O,c}$ are the anodic and cathodic activation fluxes (thermodynamic fluxes) for reduction reactions, respectively. α_M and α_O are the charge transport coefficients for the oxidation reaction and reduction reaction, respectively. $\tilde{A}_M$ and $\tilde{A}_O$ are the electrochemical affinity (thermodynamic force) for oxidation and reduction reactions induced by the electrochemical potential, respectively. The chemical affinity $\tilde{A}$ is defined as $\tilde{A} = z\eta F = zF(E - E_{corr})$ (Gutman, 1998). F is Faraday's constant, η is the overpotential defined as $\eta = E - E_{corr}$, in which E_{corr} is the equilibrium electrode potential (corrosion potential), and E is the potential applied on the working electrode (steel sample). Finally, t_{corr} is the corrosion time.

The activation fluxes can be calculated based on the Butler-Volmer equation, given by Lim (2014); Page (2007); Popov (2015),

$$J_M = J_{M,a} + J_{M,c} = j_M^0\left[\exp\left(\frac{\alpha_{M,a}\tilde{A}_M}{RT}\right) - 1\right] - j_M^0\left[\exp\left(\frac{-\alpha_{M,c}\tilde{A}_M}{RT}\right) - 1\right] \tag{58}$$

$$J_{O,a} = J_{O,a} + J_{O,c} = j_R^0\left[\exp\left(\frac{\alpha_{O,a}\tilde{A}_O}{RT}\right) - 1\right] - j_R^0\left[\exp\left(\frac{-\alpha_{O,c}\tilde{A}_O}{RT}\right) - 1\right] \tag{59}$$

In the above equations, j_0 is the exchange flux which is a function of the concentrations of the reduced and oxidized species:

$$j_0 = F(k_c C_O)^{\alpha}(k_a C_R)^{1-\alpha} \tag{60}$$

where k_a and k_c are the anodic and cathodic reaction rate constants, respectively. C_O and C_R are the concentration of oxidized and reduced species, respectively. To compute the entropy production numerically using Eq. (57), the charge transfer coefficients, corrosion potential, and corrosion current densities must be obtained from the potential (V) versus current (A) Tafel test measurement.

Entropy Generation due to Electrochemical Reaction Overpotential

The entropy production due to chemical reaction overpotential is given by

$$\Delta S_{react} = \frac{1}{T}\int_{t_0}^{t}\left(\sum_{j=1}^{r}\upsilon_j A_j\right)dt_{corr} \tag{61}$$

where r is the number of chemical reactions involved, T is the absolute temperature, υ_j is the chemical reaction rate in units of mol s^{-1}, and A_j is the chemical reaction affinity in the units of kJ mol^{-1}.

Typically, the contribution of chemical reaction overpotential is smaller than the activation overpotential mechanism if only a few chemical species interact in the corrosive environment. The calculation of Eq. (61) requires the determination of chemical reaction rate and chemical affinity. In this model, entropy production due to corrosion focuses only on the simple redox reaction when metal is submerged in the salt solution, as follows.

On the anode side, loss of electrons occurs

$$\mathrm{Fe} \leftrightarrow \mathrm{Fe}^{2+} + 2e^-$$

On the cathode side, the evolution of dissolved oxygen

$$\mathrm{O_2} + 2\mathrm{H_2O} + 4\mathrm{e}^- \longleftrightarrow 4(\mathrm{OH})^- \tag{62}$$

Therefore, the number of chemical reactions involved r in this case is equivalent to 2. We use the chemical reaction rate υ and electrochemical affinity $\tilde{A}$ of metal dissolution and dissolved oxygen reduction to estimate entropy production. However,

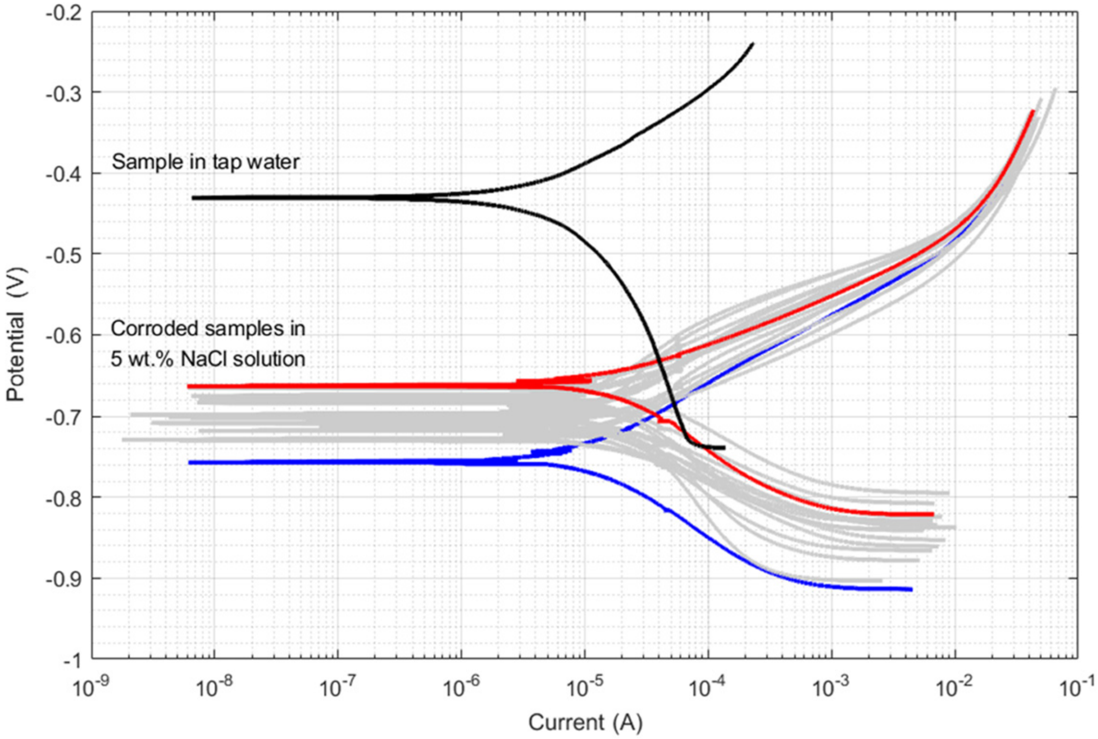

Fig. 13 Tafel plot of the 16 samples (after corrosion immersion for 20 days) in 5 wt% NaCl solution.

calculating the reaction rate υ, requires parameters such as reaction rate constants k_a, k_c, and the concentration of oxidized and reduced species C_O and C_R, respectively (Lim, 2014; Page, 2007; Popov, 2015).

Electrochemical Corrosion Tests

The corrosion reaction measurements are required for determining some electrochemical material constants. They are measured by a potentiostat (Fakhri *et al.*, 2019; Refait *et al.*, 2020; Eyu *et al.*, 2016; Komalasari *et al.*, 2020), which is a three-electrode system composed of a reference electrode (RE), a counter electrode (CE), and a working electrode (WE). **Fig. 12** shows the setup of the electrochemical cell, in which the central test specimen (A656 grade steel) is the working electrode (WE), a rolled-up stainless steel wire mesh encircling the test sample is the counter electrode (CE), and a saturated copper-copper sulfate electrode (CSE) is the reference electrode (RE) (Zhang *et al.*, 2021; Roberts, 1954; Bard *et al.*, 2022). **Fig. 13** shows an example of the potential vs. current Tafel plot, measured after the sample is corroded in the salt solution for 20 days. **Table 1** shows an example output from the potentiostat.

Fatigue Life Estimation for Pre-Corroded Samples Subjected to Ultrasonic Vibration Fatigue

The thermodynamic state index for a pre-corroded sample subjected to ultrasonic vibration fatigue can be written as

$$\Phi = 1 - \exp\left[-m_s(\Delta s_{act} + \Delta s_{react} + \Delta s_T + \Delta s_r + \Delta s_{mp})/R\right] \tag{63}$$

Fig. 14. shows the entropy generation and TSI evolution for the corrosion process, respectively. **Fig. 15** shows entropy generation and TSI evolution for the following ultrasonic vibration test, performed using the pre-corroded samples, respectively.

In **Fig. 16**, it is shown that the corrosion degradation of the steel results in a decrease in fatigue life. According to the simulation, when the stress amplitude is at 400 MPa, the fatigue life decreases from $2.79 \cdot 10^6$ cycles to $1.58 \cdot 10^6$ cycles due to the corrosion degradation, which is around a 40 % reduction in fatigue life. The corrosion degradation also changes the fatigue failure fracture mechanisms. For uncorroded samples, ductile fracture happens at high fatigue stress amplitude while brittle fracture only happens at low-stress amplitude. For the pre-corroded sample, brittle failure was found at all mean stress amplitudes. A more detailed fractographic analysis of the pre-corroded sample based on SEM images can be found in Lee *et al.* (2022b).

Table 1 Example output from the Tafel test

Set	*Corrosion time*	β_A *(V/decade)*	β_C *(V/decade)*	*Icorr* (μ*A)*	*Ecorr (mV)*	*Corr rate* (μ*py)a*
3	40 days	0.1140	0.0789	65.6692	−706.3846	473.2154

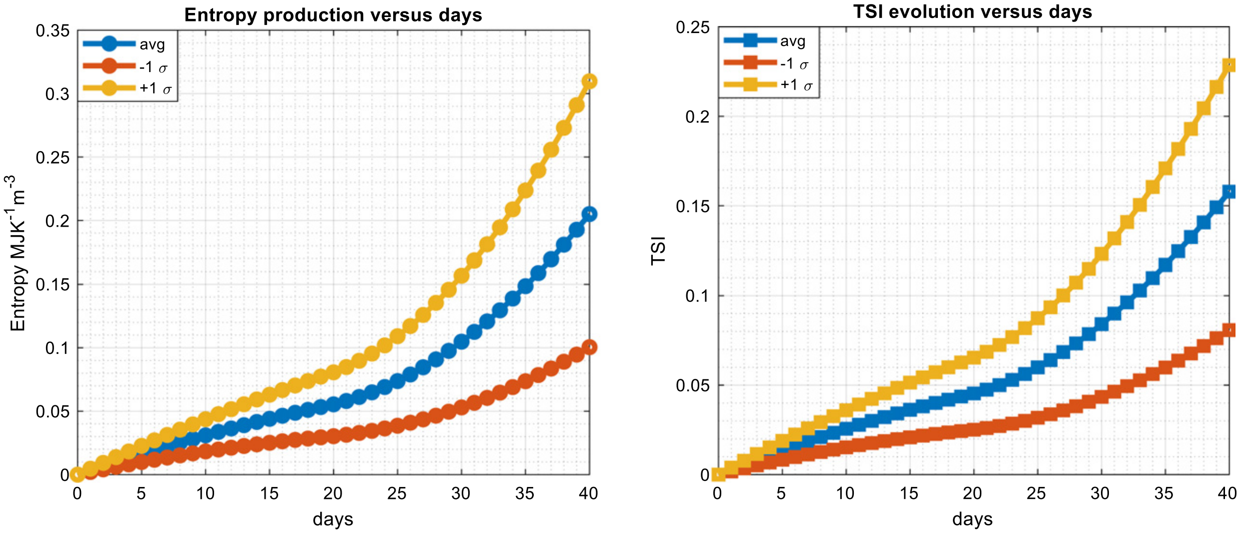

Fig. 14 Cumulative entropy production (left) and TSI evolution (right) versus days during the 40-day corrosion immersion, due to both activation overpotential and chemical reaction overpotential. The three branches in each graph show the lower bound and upper bound of the entropy production because the electrochemical constants used in the model are mean values of 16 samples tested.

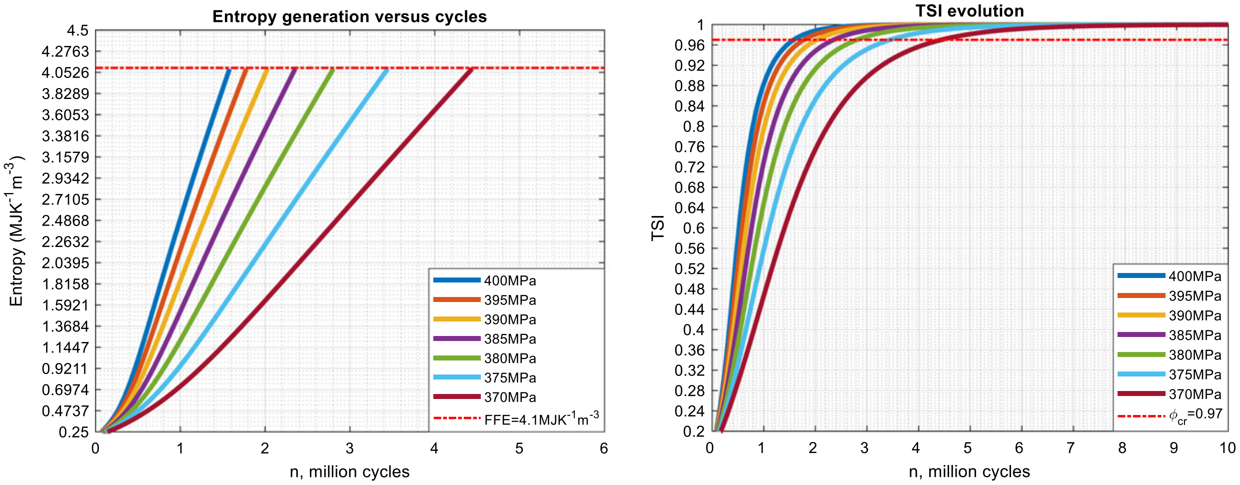

Fig. 15 Cumulative entropy production (left) and TSI evolution (right) for the corroded sample during ultrasonic vibration fatigue. It should be noted that both the entropy and the TSI do not start from zero, because pre-corrosion induces entropy production and TSI evolution before the fatigue test.

Modeling Fatigue Life and Hydrogen Embrittlement of BCC Steel With Unified Mechanics Theory

The reliability of metallic alloys operating in hydrogen-rich environments such as hydrogen pipelines, hydrogen-burning internal combustion engines, etc. is important. Studies in the past 40 years have shown that the diffusion of hydrogen into steel and other metals causes various chemical reactions, hydrogen-material interactions, and microstructural changes. These physical-chemical

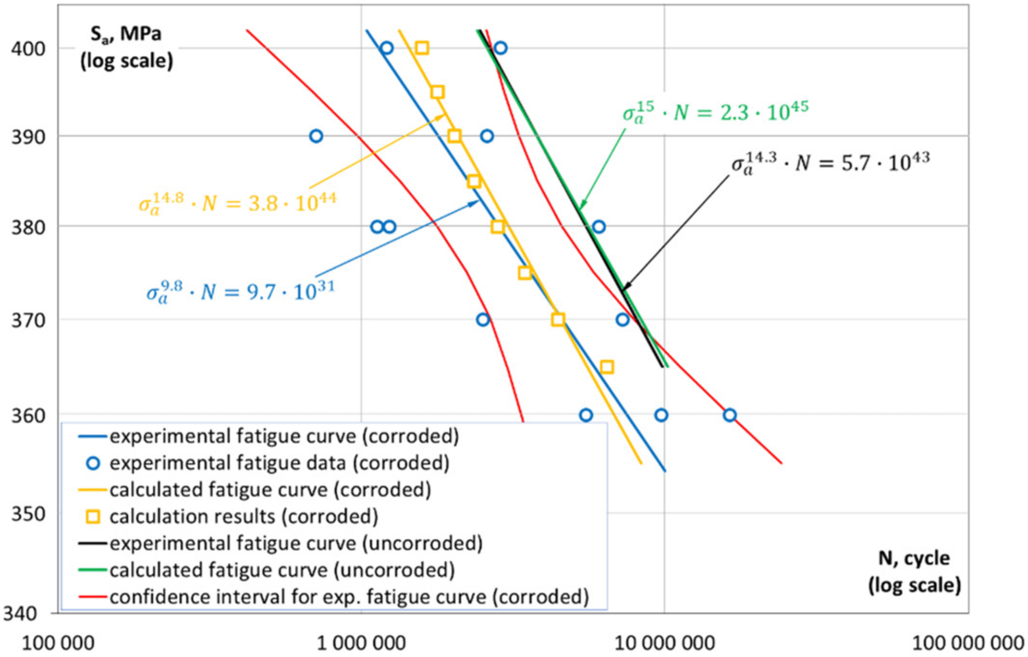

Fig. 16 Comparison of experimental data with model simulations of the mean stress vs. the number of cycles (S-N) curves for the pre-corroded and uncorroded samples.

changes in the material include hydrogen embrittlement (HE), and hydrogen environmentally assisted cracking (HEAC). In particular, hydrogen embrittlement mechanisms, such as hydrogen-enhanced localized plasticity (HELP) and hydrogen-enhanced decohesion (HEDE) can have synergetic effects in steel depending on the hydrogen concentration level. At concentrations above and below the critical hydrogen concentration level, HEDE and HELP dominate the embrittlement process, respectively. Different HE mechanisms result in distinctly different fracture modes, both ductile and fully brittle. In this section, modeling the ultrasonic vibration fatigue life of bcc steel with a ferrite-pearlite microstructure pre-charged with hydrogen at different concentrations is presented based on the UMT. The synergetic interaction of hydrogen embrittlement mechanisms in steel and other metallic materials, i.e., HELP and HEDE at different hydrogen concentrations (HELP + HEDE model of HE) is also presented. Modeling the synergetic effects between ultrasonic vibration fatigue life and synergistically active hydrogen embrittlement mechanisms in low carbon bcc steel (S355J2 +N, equivalent to ASTM A656), according to the HELP + HEDE model for HE, using UMT is presented.

Based on the UMT, the degradation in hydrogen pre-charged steel during ultrasonic vibration is quantified by the thermodynamic state index. The entropy production mechanisms for hydrogen pre-charged steel subjected to ultrasonic vibration can be classified into three distinct categories (Lee *et al.*, 2023):

1) ΔS_{corr}, is the entropy production due to the electrochemical reaction with hydrogen during the hydrogen pre-charging,
2) ΔS_{mec}, is the entropy production due to mechanical loading (ultrasonic vibration),
3) ΔS_{he}, is the entropy production due to hydrogen-enhanced mechanisms (the synergy of HELP and HEDE mechanism of HE according to the HELP + HEDE model) and other types of hydrogen-metal interactions and hydrogen damage mechanisms.

The focus of this section is on ΔS_{he}, which is composed of five entropy generation mechanisms.

$$\Delta S_{he} = \Delta S_{mp} + \Delta S_{hede} + \Delta S_{dl} + \Delta S_{ht} + \Delta S_{hcoup} \tag{64}$$

Where ΔS_{mp}, ΔS_{hede}, ΔS_{dl}, ΔS_{ht}, and ΔS_{hcoup} are entropy generations due to hydrogen-enhanced localized microplasticity (HELMP), the HEDE process of HE, work of hydrogen-induced lattice dilatation, hydrogen transport, and the coupling of microplastic strain with transient hydrogen concentrations, respectively. In the following subsections ("Entropy Generation Due To Hydrogen-enhanced Micro-plasticity (HELMP)"– "Entropy Generation Due To Hydrogen-enhanced Decohesion"), the formulation for two ΔS_{he} entropy generation mechanism, i.e., ΔS_{mp} and ΔS_{hede}, are discussed in detail. The other three terms presented in Eq. (64) are omitted because they have negligible entropy generation contributions (Lee *et al.*, 2023).

Entropy Generation due to Hydrogen-Enhanced Micro-Plasticity (HELMP)

The hydrogen-enhanced microplasticity model used here has the same form as Eq. (49) with a different microplastic strain increment scheme than Eq. (38). The activated lattice defect sites that lead to stress localization during ultrasonic vibration are

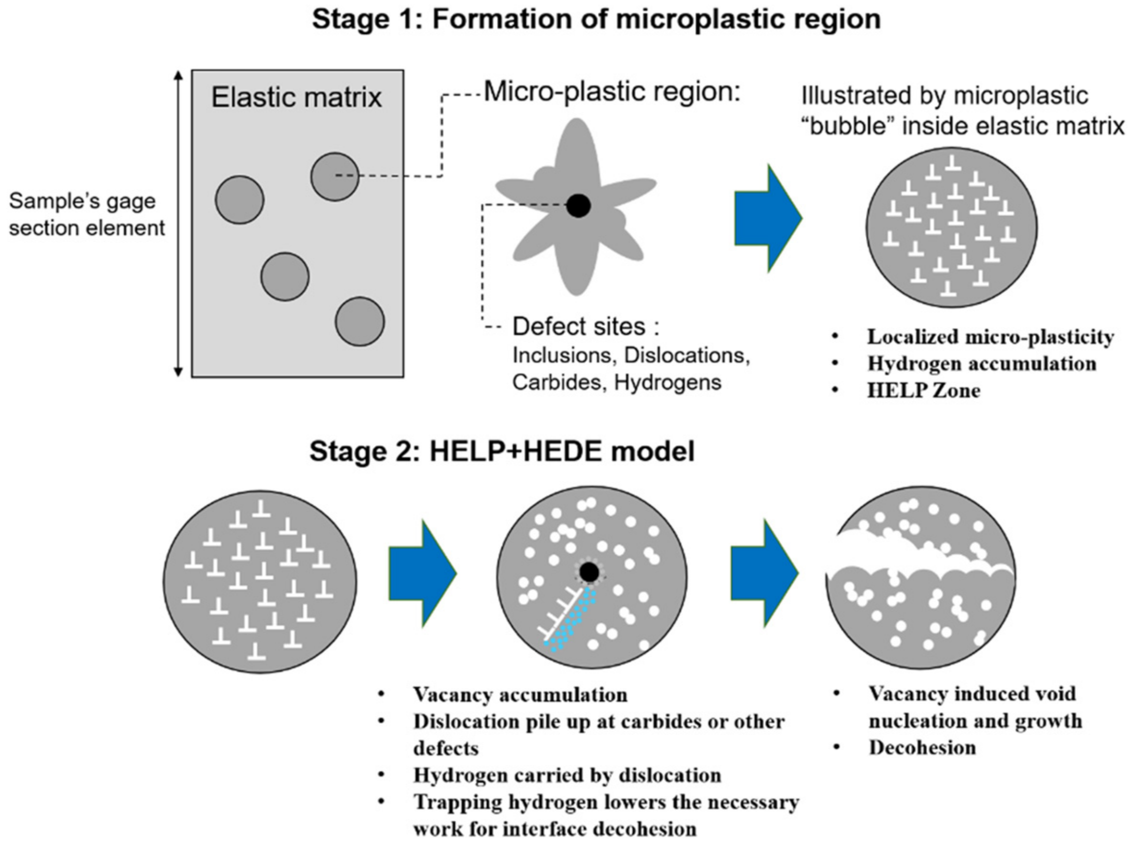

Fig. 17 Illustration of the synergy of hydrogen-enhanced microplasticity (HELPM) and hydrogen-enhanced decohesion (HEDE) (Lee *et al.*, 2023), HELP + HEDE model for HE (Djukic *et al.*, 2019, 2015, 2016a; Wasim *et al.*, 2021), during high cycle fatigue.

inclusions, vacancies, and dislocations. In the presence of hydrogen, the term "defect" also includes the interstitial and trapped hydrogen atoms. For the HELP mechanism of HE, the increasing concentration of hydrogen at trapping sites specifically in the Cottrell field of the dislocation decreases the activation energy for dislocation motion, increasing the deformation in localized regions near the fracture surface (Robertson *et al.*, 2015; Martin *et al.*, 2019). Assuming the microplastic strain ε_P^μ is enhanced by the hydrogen concentration through the same function proposed by (Novak, 2009; Novak *et al.*, 2010), the hydrogen-enhanced plastic strain rate $\dot{\varepsilon}_P^\mu$ can be expressed by the following relation:

$$\dot{\varepsilon}_P^\mu = \dot{\varepsilon}_0 \sinh\left[\tilde{\Psi}\left(\frac{\sigma_e^\mu}{\tilde{\gamma}+\kappa^\mu}-1\right)^n\right]\frac{\sigma^{\mu'}}{\sigma_e^\mu} \tag{65}$$

Where $\tilde{\Psi}$ is a positive dimensionless slip activation energy parameter as a decreasing function of hydrogen concentration, which is used to account for the effect of the activation energy required for dislocation motion. $\dot{\varepsilon}_0$ is a reference strain rate, σ_e^μ is the von Mises effective micro-stress, $\sigma^{\mu'}$ is the deviatoric micro-stress tensor,and $\tilde{\gamma}$ is the initial micro-yield stress of the material, as a function of hydrogen concentration. n is the hardening exponent, and κ^μ is the microflow stress over and above the initial micro-yield stress. The evolution of the flow stress is given by

$$\dot{\kappa}^\mu = \left[\tilde{H} - \tilde{R}\cdot\kappa^\mu\right]\dot{\varepsilon}_p^\mu \tag{66}$$

where $\tilde{H}$ is the hardening coefficient and $\tilde{R}$ is the dynamic recovery coefficient, both are functions of hydrogen concentration.

The material parameters as a function of hydrogen concentration in trapping sites, C_T in Eqs. (65) and (66) are assumed to have the following linear relations (Novak, 2009; Novak *et al.*, 2010),

$$\tilde{\Psi}(C) = \Psi_0\left(1+\Psi_c\frac{C_T}{C_0}\right);\ \tilde{\gamma}(C) = \gamma_0\left(1+\gamma_c\frac{C_T}{C_0}\right);\ \tilde{H}(C) = H_0\left(1+H_c\frac{C_T}{C_0}\right) \tag{67}$$

where C_T/C_0 is the normalized hydrogen concentration in trapping lattice sites, C_0 is the maximum possible range of C_T. Ψ_c, γ_c, and H_c are positive dimensionless constants representing the hydrogen-induced plastic softening, the blocking of Frank-Read dislocation sources by hydrogen, and the hydrogen-assisted hardening, respectively (Novak, 2009). They can be experimentally measured by pre-charging a test sample to $C_T = C_o$ level, then obtaining $H_c = (\tilde{H} - H_0)/H_0$ when $C_T = C_0$.

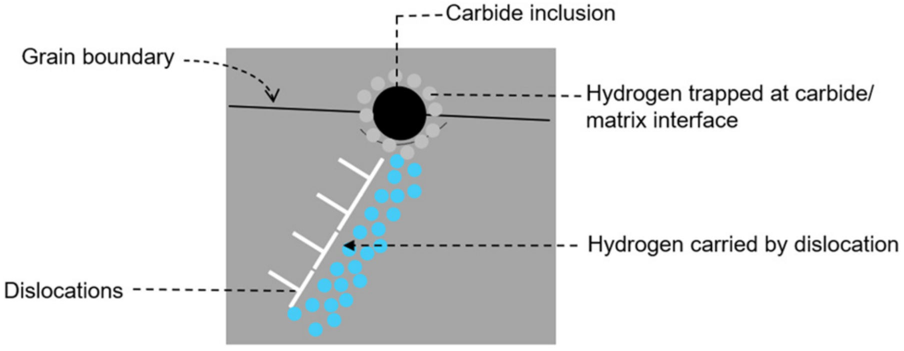

- Initiated by a dislocation pile-up against a grain-boundary carbide
- Leads to interface decohesion and intergranular fracture

Fig. 18 Illustration of the HEDE interaction between hydrogen and dislocation, adapted from Novak, 2009; Novak *et al.*, 2010; Li *et al.*, 2020).

Entropy Generation due to Hydrogen-enhanced Decohesion

If hydrogen concentration in the sample is above the critical value, such that the HEDE mechanism takes place and becomes prevalent, we assume that the HELP and HEDE mechanisms happen simultaneously (HELP + HEDE) at the same defect sites (i.e., vacancies, inclusions, dislocations cross-slips, or hydrogen solute atoms) (Novak, 2009; Novak *et al.*, 2010; Li *et al.*, 2020). **Fig. 17** illustrates the two-stage model for the formation of the microplasticity region (stage I), and the synergy of hydrogen-enhanced microplasticity (HELPM) (Lee and Basaran, 2022; Lee *et al.*, 2022a,b, 2023) and hydrogen-enhanced decohesion (HEDE), according to the HELP + HEDE model for HE by Djukic *et al.* (2019); Popov *et al.* (2018); Djukic *et al.* (2015, 2016a); Wasim *et al.* (2021); Wasim and Djukic (2020); Djukic *et al.* (2014, 2016b) (stage II) during high cycle fatigue (Lee *et al.*, 2023). The stress in the microplastic region is below the macroscopic yield stress.

According to HELP mediated HEDE model for HE (Robertson *et al.*, 2015; Martin *et al.*, 2019), hydrogen facilitates dislocation movements due to the HELP mechanism and leads to high-density dislocation pile-up (Novak, 2009; Novak *et al.*, 2010; Nagao *et al.*, 2018). As a result of hydrogen-enhanced dislocation movement, the hydrogen trapped and transported by dislocations increases hydrogen concentration at the carbides (Novak, 2009; Novak *et al.*, 2010), as shown schematically in **Fig. 18**, grain boundary (Nagao *et al.*, 2018) and other defect sites acting as dislocation barriers, leading to the interface decohesion due to HEDE activation (Djukic *et al.*, 2019; Popov *et al.*, 2018; Djukic *et al.*, 2015, 2016a; Wasim *et al.*, 2021; Wasim and Djukic, 2020; Djukic *et al.*, 2014, 2016b), see **Figs. 17** and **18**. Therefore, the synergistic effect of HELP and HEDE mechanisms leads to the brittle hydrogen-assisted fracture and microstructural evolution under intergranular fracture (Robertson *et al.*, 2015; Martin *et al.*, 2019; Novak, 2009; Novak *et al.*, 2010; Djukic *et al.*, 2019; Popov *et al.*, 2018; Djukic *et al.*, 2015, 2016a; Wasim *et al.*, 2021; Djukic *et al.*, 2014, 2016b; Nagao *et al.*, 2018).

The decohesion entropy generation due to the hydrogen-enhanced decohesion (HEDE) mechanism of HE ΔS_{hede} is given by the following relation,

$$\Delta S_{hede} = \int_{t_0}^{t} \Phi f_v h_{a/v} \frac{\dot{\gamma_p}}{T} dt \tag{68}$$

Where, Φ is the thermodynamic state index, $f_v$is the volume fraction of activated micro defects, $h_{a/v}$ is the surface area to volume ratio, used to convert the entropy unit from $J/(K{\cdot}m^2)$ to $J/(K{\cdot}m^3)$ and $\dot{\gamma_p}$ is the rate of plastic work of the decohesion process, T is the absolute temperature. Assuming the carbide particles that result in decohesion at a carbide/matrix interface are all spherical, $h_{a/v} = 4.84$. $\dot{\gamma_p}$ is a function of interface hydrogen coverage as well as thermodynamic parameters. A detailed discussion of $\dot{\gamma_p}$ can be found in Lee *et al.* (2023), therefore we do not repeat the mathematical derivation here.

Fatigue Life Estimation for Hydrogen Embrittled Steel Subjected to Ultrasonic Vibration Fatigue

The thermodynamic state index evolution for ultrasonic vibration fatigue of pre-hydrogen embrittled steel can be given by

$$\Phi = 1 - \exp\left[-\frac{m_s}{R}(\Delta s_{corr} + \Delta s_{mec} + \Delta s_{he})\right] \tag{69}$$

In which Δs_{mec} is the specific entropy generation due to elastic fatigue loading discussed in Sections "Predicting High Cycle Fatigue Life with Unified Mechanics Theory" and "Modeling Ultrasonic Vibration Fatigue", Δs_{corr} is the specific entropy generation due to corrosion discussed in Section "Modeling Fatigue of Pre-Corroded Body-Centered Cubic Metals with Unified Mechanics Theory", and Δs_{he} is the specific entropy generation due to hydrogen-enhanced mechanisms, i.e., simultaneously active HE mechanisms such as HELP and HEDE (HELP + HEDE) discussed in Section "Modeling Fatigue Life and Hydrogen Embrittlement of BCC Steel with Unified Mechanics Theory". **Fig. 19** shows the contribution of entropy generation from elastic fatigue loading and hydrogen embrittlement, mechanisms. It is verified that hydrogen-enhanced entropy production mechanisms other than due

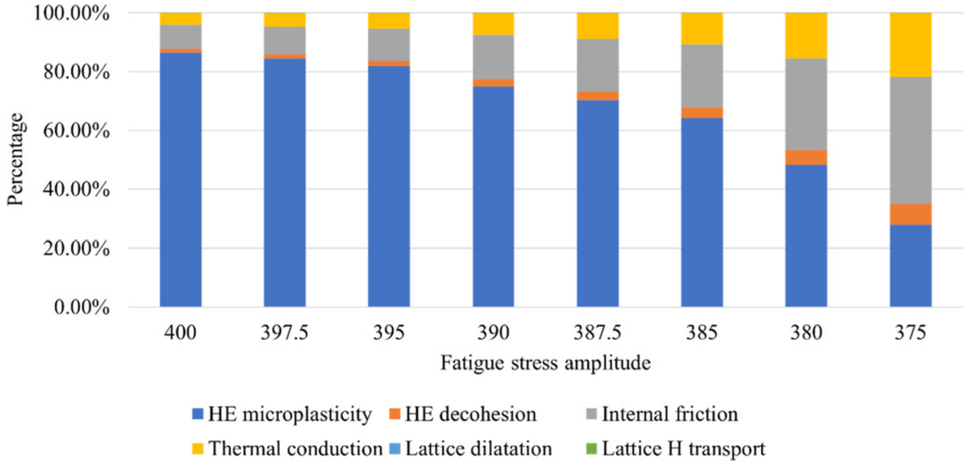

Fig. 19 The entropy contribution percentage of each mechanism under different vibration mean stress amplitudes, considering $C_T = 0.5C_0$.

to the HELP (HE microplasticity) and HEDE (HE decohesion) mechanisms of HE are negligible (Lee *et al.*, 2023). The entropy generation due to internal friction and thermal conduction, in the category of elastic fatigue loading, are also as important as HELP and HEDE. **Fig. 19** does not include corrosion entropy production because the corrosion mechanism is not activated concurrently with elastic fatigue loading and hydrogen embrittlement. [it is assumed that the sample is pre-corroded and then subjected to cycling fatigue loading]. However, corrosion entropy generation is non-negligible since it gives initial TSI evolution before the elastic fatigue and the hydrogen embrittlement.

Based on the TSI evolution equation for the pre-hydrogen charged sample under ultrasonic vibration, we can establish the simulated S-N curve, as shown in **Fig. 20**. From **Fig. 20**, we observe that the fatigue life of hydrogen pre-charged steel is reduced compared to the reference sample (no pre-corrosion or pre-HE). The fatigue life reduction from the reference sample to $C_T = 0.05C_0$ sample mainly results from the decrease of microscopic yield stress due to corrosion damage during hydrogen pre-charging. As for the comparison between three hydrogen-charged samples at different H-trapping concentrations $(C_T = 0.05, 0.25, \text{and } 0.5C_0)$, the reason for fatigue reduction is because of the increasing trapped hydrogen concentration C_T induces greater hydrogen-enhanced localized microplastic strain (HELMP), according to Eq. (67). However, meanwhile, the hardening modulus $\tilde{H}$ and yield stress $\tilde{y}$ are slightly increased due to higher C_T that cause the material to become more brittle and less ductile. Therefore, higher trapped hydrogen concentration does not lead to fatigue life reduction, particularly at fatigue stress amplitudes below 395 MPa, see S-N curves for higher $C_T = 0.5C_0$vs $C_T = 0.25C_0$ shown in **Fig. 20**.

It should also be emphasized that this result only applies to ultrasonic vibration fatigue, which operates at 20 kHz cyclic loadings within the material's linear elastic range. Because according to the presented model, the density of hydrogen trapping sites at dislocations is assumed to remain constant at various fatigue stress amplitudes (Lee *et al.*, 2023). This assumption lowers the contribution from the HEDE mechanism of HE, compared to low cycle fatigue, where material experiences microplasticity.

Low Cycle Fatigue Life Prediction

Material degradation is a manifestation of internal energy dissipation. In Newtonian continuum mechanics, degradation evolution is modeled using empirical functions obtained by curve fitting a function to degradation test data. Using such an approach, the thermodynamic consistency is lost and also, and the models become case specific, (for example the degradation evolution function/potential obtained from a low-frequency loading does not apply to high-frequency loading). Empirical evolution functions often require dozens of curve-fitting parameters with no physical meaning as the number of dissipative mechanisms increases.

The rate-independent stress-strain response of metals undergoing plastic deformation can be formulated as follows. In the absence of kinematic hardening, the following additive decomposition of the Helmholtz free energy function is assumed,

$$\Psi(\varepsilon^e, h;\Phi) = \Psi^E(\varepsilon^e;\Phi) + \Psi^I(h,\Phi) \tag{70}$$

where, Ψ^{E} is the elastic strain energy and Ψ^{I} is the free energy from the isotropic hardening. In Eq. (70), the hardening flux parameter h evolves with plastic strain. Using Eq. (70), Eq. (79), and generalized Hooke's law, the following form of free energy is obtained,

$$\Psi(\varepsilon^e, h;\Phi) = \frac{1}{2}(1-\Phi)\left(\lambda\varepsilon^e_{kk}\varepsilon^e_{mm} + 2\mu\varepsilon^e_{ij}\varepsilon^e_{ij}\right) + (1-\Phi)\frac{1}{r}Kh^{r+1} \tag{71}$$

A power-law model for isotropic hardening is assumed, where K, and r, are the isotropic hardening material parameters, Φ is the thermodynamic state index, λ and μ are the lame's constants, ε^e is the elastic strain tensor. The material model used in this

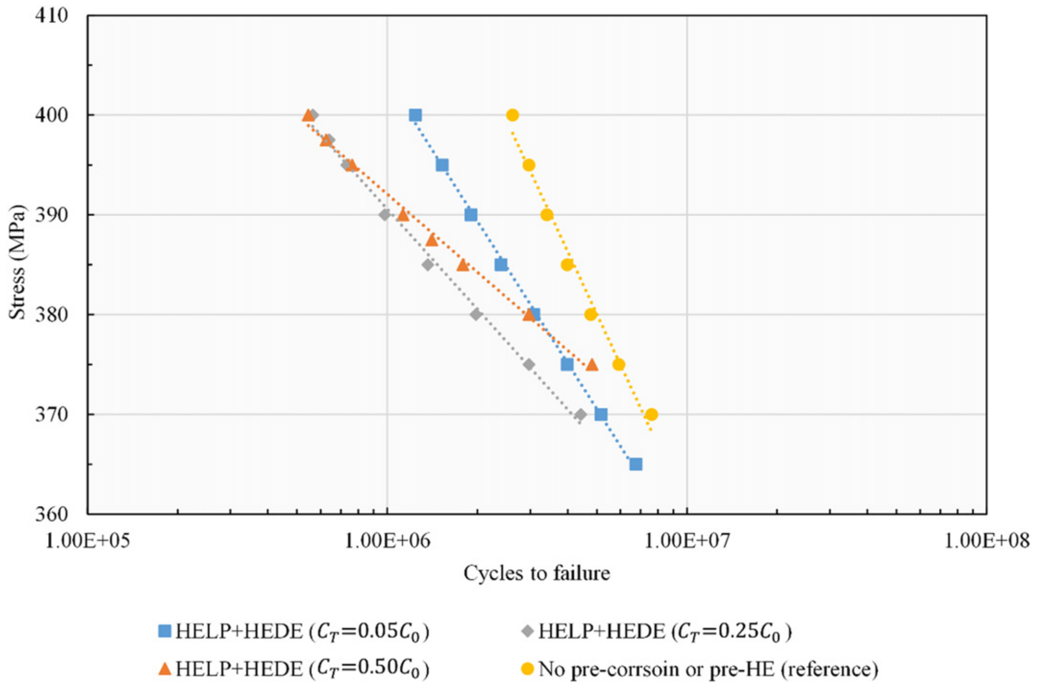

Fig. 20 Unified mechanics theory-based simulated ultrasonic vibration fatigue S-N curves for the hydrogen pre-charged S355J2 + N steel samples (HELP + HEDE model) at different hydrogen trapping concentration levels C_T compared to the reference sample.

numerical model is independent of the strain rate and the temperature and hence the strain rate hardening behavior and temperature effects, including the thermal dissipation are not considered. The conjugate force is given by

$$\sigma = \rho \frac{\partial}{\partial \varepsilon^e} \Psi \tag{72}$$

Where σ is the stress tensor, ρ is the mass density. The following yield function is used for the example titanium alloy Ti-6Al-4 V simulated here

$$\mathscr{F}^p(\sigma, H;\Phi) = \sigma'_{eq} - \left(\sigma_{y_o} + H\right) \tag{73}$$

where, σ'_{eq} are the Von-Mises equivalent of stress, σ_{y_o} represents the initial yield stress and H represents the hardening stress. Using the normality rule, the plastic strain rate $\dot{\varepsilon}^p$ is given by the following equation.

$$\dot{\varepsilon}^p_{ij} = \dot{\Gamma}\left[\frac{1}{(1-\Phi)} \frac{3}{2} \frac{S'_{ij}}{\sigma'_{eq}}\right] \tag{74}$$

where, $\dot{\Gamma}$ is the consistency parameter, S is the deviatoric stress tensor. We write the norm of the plastic strain rate to quantify the consistency parameter, $\dot{\Gamma}$,

$$\dot{\varepsilon}^p_{eq} = \sqrt{\frac{2}{3} \dot{\varepsilon}^p_{ij} \dot{\varepsilon}^p_{ij}} = \dot{\Gamma} \frac{1}{(1-\Phi)} \tag{75}$$

We can define the following relationship between $\dot{h}$ and $\dot{\varepsilon}^p_{ij}$, which stipulates that isotropic hardening will decrease as degradation increases according to the second law of thermodynamics.

$$\dot{h} = \dot{\varepsilon}^p_{eq}(1-\Phi) \tag{76}$$

During low-frequency low-cycle fatigue loading there are six entropy generation mechanisms. Under low strain rate loading at low cycle fatigue loading the largest entropy generation is generated by the plastic work. Other entropy generation mechanisms' magnitudes are smaller by orders of magnitude. Accumulated specific entropy at the n$^{\text{th}}$ strain increment is computed as follows,

$$\Delta s_n = \frac{1}{\rho T} \sum_{i=1}^{i=n} \sigma_i : \Delta \varepsilon^p_i \tag{77}$$

Where, Δs_n is the accumulated specific entropy, ρ is the mass density, T is the temperature, σ is the stress, and ε^{p} is the plastic strain. In Eq. (77), the incremental TSI is calculated as follows,

$$\Phi_{i+1} = \Phi_c\left[1 - \exp\left(-\Delta s_i \frac{m_s}{R}\right)\right] \tag{78}$$

Where, Φ_{c} is the critical TSI value. The constitutive relation in simplified form can be written as follows,

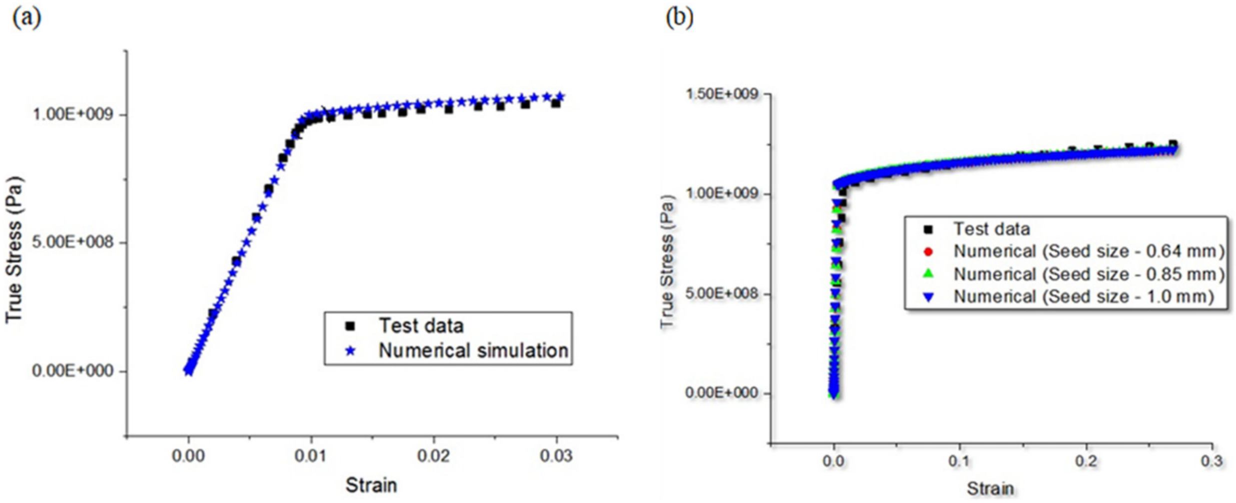

Fig. 21 Monotonic (a) tensile and (b) compressive stress-strain graphs.

$$\sigma_{ij} = (1-\Phi)\mathscr{C}^{0}_{ijkl}\varepsilon^{e}_{kl} \tag{79}$$

Where, σ_{ij}, and ε^{e}_{kl} are the stress and strain tensors in indicial representation. The tangential constitutive tensor $\mathscr{C}_{ijkl}$ is related to the virgin state of the material.

Using ABAQUS user-defined material model subroutine option, Eq. (72) through Eq. (76) are solved. The constitutive model is implemented to simulate monotonic stress-strain responses as shown in **Fig. 21** for the Ti-6Al-4 V alloy ASTM standard-size sample.

Using a three-dimensional model, the low cycle fatigue life of Ti-6Al-4 V alloy is simulated. Total strain amplitude versus the number of cycles is shown in **Fig. 22** for the test data, 1-D analytical model, and 3-D model simulation results. The 3D model's number of cycles to the failure simulation data point is not shown for the total strain of 0.008, because of the extensive computation time required. Details of the simulation are given in Bin Jamal *et al.* (2019).

Single Crystal Plasticity-Based Thermodynamically Consistent Flow-Stress Model

Consider a single crystal body $\mathscr{B}$ as the reference configuration whose material point is $\mathscr{P}$, then the motion of the material point is defined by,

$$x = \gamma(X, t) \tag{80}$$

Where, X and x are the material coordinates of the body, B in the reference configuration and current configuration, respectively. The slip, $\mathbb{S}^{\alpha}_{0}$ in the single crystal lattice is defined by the Schmid tensor as follows,

$$\mathbb{S}^{\alpha}_{0} = s^{\alpha}_{0} \otimes m^{\alpha}_{0} \tag{81}$$

Where, s^{α}_{0} and m^{α}_{0} are the slip directions and slip plane normal, respectively, for slip plane α, where $\alpha = 1, 2, 3\ldots$ N number of slip systems with each local slip rate, $\dot{\Upsilon}^{\alpha}$. Using the elastic-plastic decomposition of the deformation gradient, and Eq. (81), the following equation is obtained for the velocity gradient, L of the deformation.

$$L = L^{e} + F^{e}\left(\sum_{\alpha=1}^{N}\left(s^{\alpha}_{0} \otimes m^{\alpha}_{0}\right)\dot{\Upsilon}^{\alpha}\right)F^{e-1} \tag{82}$$

Where, F^{e}, and L^{e} are the elastic part of the deformation gradient and velocity gradient tensors respectively. The total internal power is given by,

$$\mathscr{P}_{\text{int}} = \mathscr{P}^{e}_{\text{int}} + \mathscr{P}^{p}_{\text{int}} \tag{83}$$

Where, $\mathscr{P}^{\text{e}}_{\text{int}}$ and $\mathscr{P}^{\text{p}}_{\text{int}}$ represent the internal elastic power and internal plastic power, respectively. The $\mathscr{P}^{\text{e}}_{\text{int}}$ can be assumed to be independent of dissipation. This assumption is not true in the strict sense of the second law of thermodynamics. However, because the elastic process dissipation is smaller than the plastic process dissipation by orders of magnitude, therefore, it is acceptable to ignore it. The external power is given by,

$$\mathscr{P}_{ext} = \int t(n).\dot{\gamma}d\hat{a} + \int f_{b}.\dot{\gamma}dV \tag{84}$$

Where, $t(n)$ and f_{b} represents surface traction acting on the differential element area, d$\hat{a}$, and the body force acting at differential volume, dV at the macro level, respectively. For a virtual displacement, $\tilde{\gamma}$, the following equation is obtained using Eq. (82).

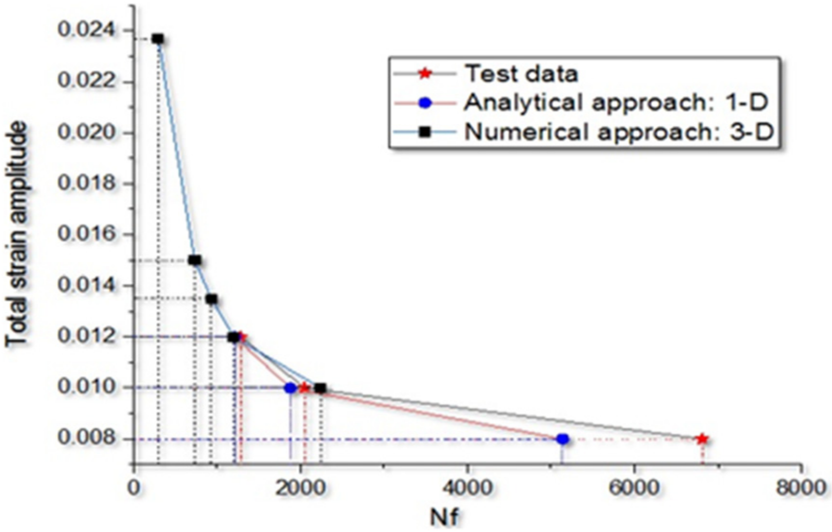

Fig. 22 Low cycle fatigue life (Nf) prediction for Ti-6Al-4 V alloy.

$$\dot{\tilde{F}}\tilde{F}^{-1} = \dot{\tilde{F}}^{e}\tilde{F}^{e} - 1 + \left(\sum_{\alpha=1}^{N} (s^{\alpha} \otimes m^{\alpha})'\dot{\tilde{\Upsilon}}^{\alpha}\right) \tag{85}$$

Where,

$$\dot{\tilde{F}} = \nabla \dot{\tilde{y}} \tag{86}$$

Hence, the total internal virtual power in Eq. (83) is given by,

$$\tilde{\mathscr{P}}_{\text{int}} = \int S^{e} : \dot{\tilde{F}}^{e} dV + \int \sum_{\alpha=1}^{N} (1 - \Phi^{\alpha}) \varkappa^{\alpha}{}'\dot{\tilde{\Upsilon}}^{\alpha} dV - \int \sum_{\alpha=1}^{N} \varkappa^{\alpha}{}'\Upsilon^{\alpha} \frac{d\Phi^{\alpha}}{d'\tilde{\Upsilon}}{}'\dot{\tilde{\Upsilon}}^{\alpha} dV \tag{87}$$

The principle of virtual power states that, $\tilde{\mathscr{P}}_{\text{int}} = \tilde{\mathscr{P}}_{\text{ext}}$. For a virtual displacement, $\dot{\tilde{y}}$, such that, $'\dot{\tilde{\Upsilon}}^{\alpha} \equiv 0$, the principle of virtual work is applied to the single crystal system. Using the frame invariance principle, the following equation is obtained for internal virtual power,

$$\mathscr{P}_{\text{int}} = \int T^{e} : \dot{E}^{e} dV + \int \sum \left(1 - \Phi^{\alpha} - {}'\Upsilon^{\alpha} \frac{d\Phi^{\alpha}}{d'\Upsilon}\right) \varkappa^{\alpha}{}'\dot{\Upsilon}^{\alpha} dV \tag{88}$$

Where, E^{e}, T^{e}, and $\varkappa^{\alpha}$ are the Green-Lagrange strain, Cauchy stress, and shear strength of each crystal slip system,α, respectively. Superscript α indicates the parameter is for a specific slip system in a single crystal. Using the principle of virtual work, the force balance equation in terms of Cauchy stress can be written as follows,

$$(\det(F)(\nabla_{x}.T)) + f_{b} = 0 \tag{89}$$

The single crystal flow rule can be given by the following relation.

$$\tau^{\alpha} = \left(1 - \Phi^{\alpha} - {}'\Upsilon^{\alpha} \frac{d\Phi^{\alpha}}{d\Upsilon}\right) \varkappa^{\alpha} sign\left({}'\dot{\Upsilon}^{\alpha}\right) \tag{90}$$

The macroscopic equilibrium Eq. (89) is to be solved using an appropriate time integration scheme, along with the micro-flow stress rule in Eq. (90) for each slip system. Using averaging scheme for Eq. (90), a single-crystal average flow stress model is derived for the high strain rate dependent mechanical response, as follows.

$$\overline{\tau} = \left(1 - \overline{\Phi}\right)\overline{\varkappa} \quad sign({}'\dot{\overline{\Upsilon}}) \tag{91}$$

Where,$\dot{\overline{\Upsilon}}$, $\overline{\tau}$, $\overline{\Phi}$, and $\overline{\varkappa}$ are the single-crystal average shear strain rate, the single-crystal average shear stress, the single-crystal average thermodynamic state index, and the single-crystal average shear resistance, respectively. The single crystal flow stress break-down in the post-yield regime is given by Voyiadjis and Abed (2005b),

$$\tau_{f} = \tau_{th} + \tau_{ath} \tag{92}$$

Where the terms τ_{f}, τ_{th} τ_{ath} represents the total flow stress, the thermal component of flow stress, and the athermal component of the flow stress, respectively. Dislocation generation, motion, annihilation, and interaction with grain boundaries have been considered, and an average micromechanics scale shear resistance model for $\overline{\varkappa}$ has been reported by Voyiadjis and Abed (2005a,b). This model is utilized here. To calculate the average TSI, $\overline{\Phi}$, in Eq. (91), various entropy generating micro mechanisms are considered at high strain rate. There are six dominant entropy generation mechanisms, in the single crystal's thermodynamic fundamental equation given below.

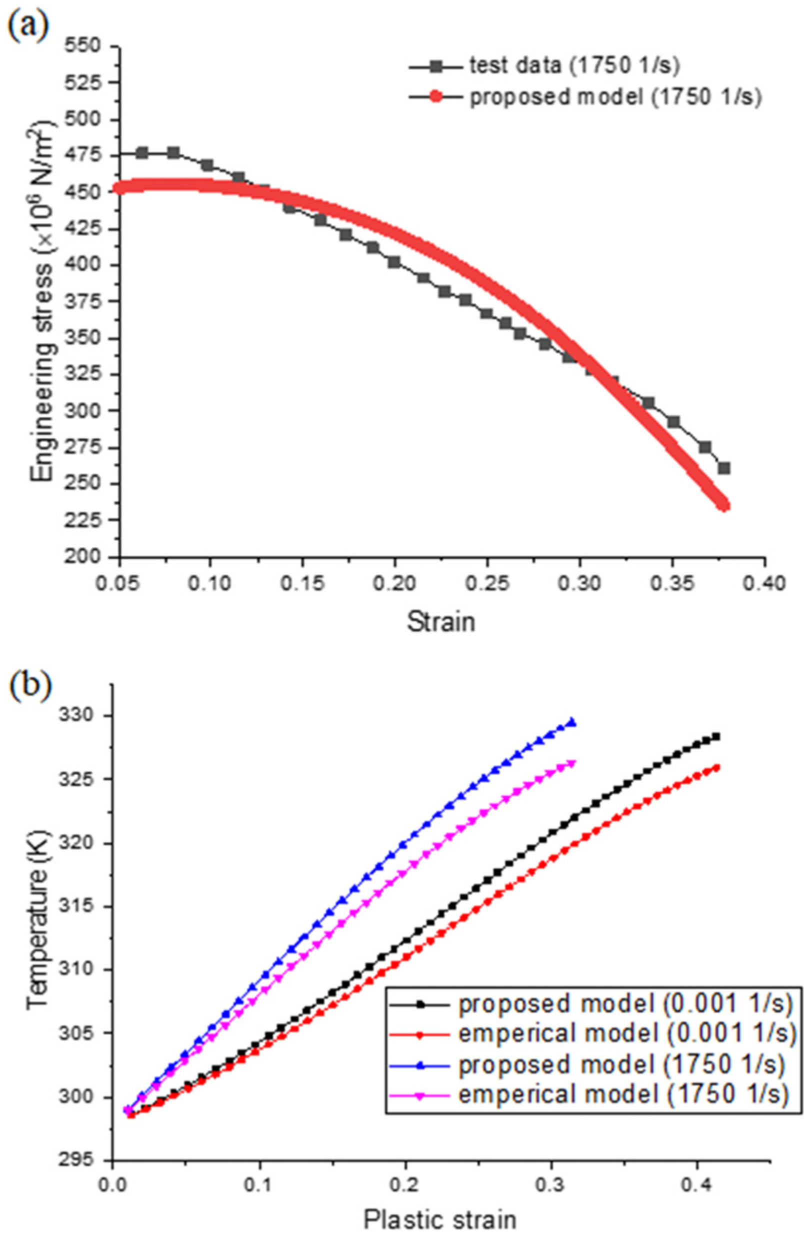

Fig. 23 Model predictions for mild steel for (a) flow stress and (b) temperature, (Bin Jamal *et al.*, 2022).

$$\Delta s_i = \frac{1}{\rho T}\left(\Delta w^{mob} + \Delta w_m^{gen} + \Delta w_{im}^{gen} + \Delta w^{an} + \Delta w_f^{n_{vac}} + \Delta w_{heat}^{\mathrm{int}}\right) \tag{93}$$

Where, ρ and T are the mass density and temperature (K), respectively. The change in specific entropy, Δs_{i} includes energy dissipations due to dislocation mobility, Δw^{mob}; mobile dislocation generation, $\Delta w_{\mathrm{m}}^{\mathrm{gen}}$; immobile dislocation generation,$\Delta w_{\mathrm{im}}^{\mathrm{gen}}$; dislocation annihilation, Δw^{an}; change in vacancy concentration due to diffusion, $\Delta w_{\mathrm{f}}^{\mathrm{n_{vac}}}$; and internal heat generation, $\Delta w_{\mathrm{heat}}^{\mathrm{int}}$. At high strain rates, there is considerable internal heat generation. At KHz loading frequency entropy generation due to internal heat generation (phonon scattering) is comparable to plastic work or can be bigger. Hence the thermo-mechanically coupled equations must be used. Using unified mechanics theory, a micromechanics-based model the fully coupled thermo-mechanical equation is derived. To estimate the energy dissipation, $\Delta w_{\mathrm{heat}}^{\mathrm{int}}$, change in temperature needs to be calculated. The change in temperature can be calculated using the unified mechanics theory based thermo-mechanical equation, as follows,

$$\Delta T = \frac{\tau_d}{\rho c_V}{}'\dot{\Upsilon}^p \Delta t + \frac{B^{drag}\varrho}{\rho c_V}\left(\frac{{}'\dot{\Upsilon}^p}{\varrho_m b}\right)^2 + \frac{1}{2}\frac{\mu b^2}{\rho c_V}\Delta\varrho - \frac{\alpha_H \mu b}{\rho c_V}\sqrt{\varrho}\,{}'\dot{\Upsilon}^p \Delta t - \ell_{eq}(T - T_0) \tag{94}$$

Where, ΔT is the change in temperature, τ_d is the crystal average shear stress, ρ is the mass density and ϱ is the dislocation density in a single crystal, c_V is the specific heat capacity, ϱ_m is the mobile dislocation density in a single crystal, T_0 is the initial temperature, α_{H} is the Taylor hardening coefficient, b is the magnitude of Burgers vector, μ is the shear modulus, and $\ell_{eq} = \frac{\Delta t}{t_{eq}}$ is the time factor to characterize the local heat loss.

This model also introduces entropy generation due to vacancy diffusion at high strain rates which is generally neglected in dislocation plasticity-based models. The model is validated for mild steel test data for a wide range of strain rates. Engineering stress-strain predictions are shown in **Fig. 23** (a) and the internal heat generation predictions are compared with Taylor-Quinney empirical model predictions as shown in **Fig. 23** (b).

Conclusions

The central focus of this chapter was to provide simple examples of using unified mechanics theory for modeling metallic materials' response without relying on empirical dissipation/degradation functions/potentials obtained from test data by curve-fitting. The dynamic equilibrium equations in unified mechanics theory do not involve any ad-hoc damping term "C". The energy loss is automatically included in the governing equations using a thermodynamic fundamental equation. The equilibrium equation in the unified mechanics theory is a function of the entropy generation, as a result, there is an additional derivative with respect to entropy that does not exist in Newtonian continuum mechanics.

Thermodynamic fundamental equations for the low cycle, high cycle, ultrasonic vibration fatigue, electrochemical corrosion, and hydrogen embrittlement metal structural materials have been derived and validated against test data,

It is shown that the thermodynamic state index can be used both at the micromechanics and continuum levels. It is shown that the TSI can be applied at different lengths and time scales.

Uncited references

Campbell and Ferguson (1970); (Gurrutxaga-Lerma *et al.*, 2015); (Huang *et al.*, 2008b); (Lin *et al.*, 2005); (Quinn, 2004); (Voyiadjis and Abed, 2005a); (Voyiadjis and Abed, 2005b).

References

Atkins, P.W., Julio De Paula, , Keeler, J., 2018. Atkins' Physical Chemistry. Oxford: Oxford University Press.
Bard, A.J., Faulkner, L.R., White, H.S., 2022. Electrochemical Methods: Fundamentals and Applications. John Wiley & Sons.
Basaran, C., 2023. Introduction to Unified Mechanics Theory with Applications, second ed. Springer. p. 2023.
Basaran, C., Nie, S., 2004. An irreversible thermodynamics theory for damage mechanics of solids. International Journal of Damage Mechanics 13 (3), 205–223. https://doi.org/10.1177/1056789504041058.
Basaran, C., Lin, M., 2007. Damage mechanics of electromigration in microelectronics copper interconnects. International Journal of Materials and Structural Integrity 1 (1/2/3), 16. https://doi.org/10.1504/ijmsi.2007.013864.
Basaran, C., Lin, M., 2008. Damage mechanics of electromigration induced failure. Mechanics of Materials 40 (1–2), 66–79. https://doi.org/10.1016/j.mechmat.2007.06.006.
Basaran, C., Lin, M., Ye, H., 2003. A thermodynamic model for electrical current induced damage. International Journal of Solids and Structures 40 (26), 7315–7327. https://doi.org/10.1016/j.ijsolstr.2003.08.018.
Bin Jamal, N.M., Rao, L., Basaran, C., 2019. Low cycle fatigue life prediction using unified mechanics theory in Ti-6Al-4V alloys. Entropy 22 (1), 24. https://doi.org/10.3390/e22010024.
Bin Jamal, N.M., Rao, L., Basaran, C., 2022. Unified mechanics theory based flow stress model for the rate-dependent behavior of bcc metals. Materials Today Communications 31. 103707. https://doi.org/10.1016/j.mtcomm.2022.103707.
Bin Jamal, N.M., Lee, H., Lakshmana Rao, C., Basaran, C., 2021. Dynamic equilibrium equations in unified mechanics theory. Applied Mechanics 2 (1), 63–80. https://doi.org/10.3390/applmech2010005.
Blaschke, D., 2019. Properties of dislocation drag from phonon wind at ambient conditions. Materials 12 (6), 948. https://doi.org/10.3390/ma12060948.
Blaschke, D.N., Mottola, E., Preston, D.L., 2019. Dislocation drag from phonon wind in an isotropic crystal at large velocities. Philosophical Magazine 100 (5), 571–600. https://doi.org/10.1080/14786435.2019.1696484.
Boltzmann, L., 1877. Über die Beziehungzwischen dem zweiten Hauptsatze des mechanischen Wärmetheorie und der Wahrscheinlichkeitsrechnung, respective den Sätzenüber das Wärmegleichgewicht. [On the relation between the second law of the mechanical theory of heat and the probability calculus with respect to theorems of thermal equilibrium]. Wiener Berichte II vol. 76, 373–435.
Burton, J.J., 1972. Vacancy-formation entropy in cubic metals. Physical Review B 5 (8), 2948–2957. https://doi.org/10.1103/physrevb.5.2948.
Cahn, R.W., Haasen, P., 1996. Physical Metallurgy. Amsterdam: North-Holland.
Callister, W.D., Rethwisch, D.G., 2020. Materials Science and Engineering: An Introduction. Hoboken, Nj: Wiley.
Campbell, J.D., Ferguson, W.G., 1970. The temperature and strain-rate dependence of the shear strength of mild steel. Philosophical Magazine 21 (169), 63–82. https://doi.org/10.1080/14786437008238397.
Charkaluk, E., Constantinescu, A., 2009. Dissipative aspects in high cycle fatigue. Mechanics of Materials 41 (5), 483–494. https://doi.org/10.1016/j.mechmat.2009.01.018.
Cugy, P., Galtier, A. (2002). Microplasticity and temperature increase in low carbon steels. In: Blom, A.F. (Ed.), Proc. 8th Int. Fatigue Congress – 3–7 June 2002. EMAS, Barnsley, pp. 549–556.
De Hosson, J., Th, M., Roos, A., Metselaar, E.D., 2001. Temperature rise due to fast-moving dislocations. Philosophical Magazine A 81 (5), 1099–1120. https://doi.org/10.1080/01418610110033975.
Djukic, M.B., Zeravcic, V.S., Bakic, G., Sedmak, A., Rajicic, B., 2014. Hydrogen embrittlement of low carbon structural steel. Procedia Materials Science 3, 1167–1172. https://doi.org/10.1016/j.mspro.2014.06.190.
Djukic, M.B., Sijacki Zeravcic, V., Bakic, G.M., Sedmak, A., Rajicic, B., 2015. Hydrogen damage of steels: A case study and hydrogen embrittlement model. Engineering Failure Analysis 58, 485–498. https://doi.org/10.1016/j.engfailanal.2015.05.017.

Djukic, M.B., Bakic, G.M., Zeravcic, V.S., Sedmak, A., Rajicic, B., 2016a. Hydrogen embrittlement of industrial components: Prediction, prevention, and models. Corrosion 72 (7), 943–961. https://doi.org/10.5006/1958.

Djukic, M.B., Bakic, G.M., Zeravcic, V.S., *et al*., 2016b. Towards a unified and practical industrial model for prediction of hydrogen embrittlement and damage in steels. Procedia Structural Integrity 2, 604–611. https://doi.org/10.1016/j.prostr.2016.06.078.

Djukic, M.B., Bakic, G.M., Sijacki Zeravcic, V., Sedmak, A., Rajicic, B., 2019. The synergistic action and interplay of hydrogen embrittlement mechanisms in steels and iron: Localized plasticity and decohesion. Engineering Fracture Mechanics 216. 106528. https://doi.org/10.1016/j.engfracmech.2019.106528.

Doudard, C., Calloch, S., Cugy, P., Galtier, A., Hild, F., 2005. A probabilistic two-scale model for high-cycle fatigue life predictions. Fatigue Fracture of Engineering Materials and Structures 28 (3), 279–288. https://doi.org/10.1111/j.1460-2695.2005.00854.x.

Eyu, G., Will, G., Dekkers, W., MacLeod, J., 2016. Effect of dissolved oxygen and immersion time on the corrosion behaviour of mild steel in bicarbonate/chloride solution. Materials 9 (9), 748. https://doi.org/10.3390/ma9090748.

Fakhri, H., Ragalwar, K.A., Ranade, R., 2019. On the use of strain-hardening cementitious composite covers to mitigate corrosion in reinforced concrete structures. Construction and Building Materials 224, 850–862. https://doi.org/10.1016/j.conbuildmat.2019.07.052.

Fan, H., Wang, Q., El-Awady, J.A., Raabe, D., Zaiser, M., 2021. Strain rate dependency of dislocation plasticity. Nature Communications 12 (1), https://doi.org/10.1038/s41467-021-21939-1.

Fan, J., Zhao, Y., Guo, X., 2018. A unifying energy approach for high cycle fatigue behavior evaluation. Mechanics of Materials 120, 15–25. https://doi.org/10.1016/j.mechmat.2018.02.001.

Fultz, B., 2010. Vibrational thermodynamics of materials. Progress in Materials Science 55 (4), 247–352. https://doi.org/10.1016/j.pmatsci.2009.05.002.

Galligan, J.M., McKrell, T.J., Robson, M.T., 2000. Dislocation drag processes. Materials Science and Engineering: A 287 (2), 259–264. https://doi.org/10.1016/s0921-5093(00)00783-8.

Gurrutxaga-Lerma, B., Balint, D.S., Dini, D., Sutton, A.P., 2015. The mechanisms governing the activation of dislocation sources in aluminum at different strain rates. Journal of the Mechanics and Physics of Solids 84, 273–292. https://doi.org/10.1016/j.jmps.2015.08.008.

Gutman, E.M., 1998. Mechanochemistry of Materials. Cambridge Int Science Publishing.

Ho, H.S., Risbet, M., Feaugas, X., 2017. A cyclic slip irreversibility based model for fatigue crack initiation of nickel base alloys. International Journal of Fatigue 102, 1–8. https://doi.org/10.1016/j.ijfatigue.2017.04.007.

Huang, M., Rivera-Díaz-del-Castillo, P.E.J., Bouaziz, O., van der Zwaag, S., 2008a. Irreversible thermodynamics modelling of plastic deformation of metals. Materials Science and Technology 24 (4), 495–500. https://doi.org/10.1179/174328408 × 294125.

Huang, M., Rivera-Díaz-del-Castillo, P.E.J., Bouaziz, O., van der Zwaag, S., 2008b. Irreversible thermodynamics modelling of plastic deformation of metals. Materials Science and Technology 24 (4), 495–500. https://doi.org/10.1179/174328408 × 294125.

Imanian, A., Modarres, M., 2015. A thermodynamic entropy approach to reliability assessment with applications to corrosion fatigue. Entropy 17 (12), 6995–7020. https://doi.org/10.3390/e17106995.

Kelly, A., Knowles, K.M., 2012. Crystallography and Crystal Defects. John Wiley & Sons.

Komalasari, Evelyn, Situmeang, I.D.R., Heltina, D., 2020. Cathodic protection on structures of carbon steel using sacrificial anode methode for corrosion control. IOP Conference Series: Materials Science and Engineering 845. 012015. https://doi.org/10.1088/1757-899x/845/1/012015.

Laughlin, D.E., Hono, Kazuhiro, 2014. Physical Metallurgy. Newnes.

Lee, H.W., Basaran, C., 2021. A review of damage, void evolution, and fatigue life prediction models. Metals 11 (4), 609. https://doi.org/10.3390/met11040609.

Lee, H.W., Basaran, C., 2022. Predicting high cycle fatigue life with unified mechanics theory. Mechanics of Materials 164. 104116. https://doi.org/10.1016/j.mechmat.2021.104116.

Lee, H.W., Basaran, C., Egner, H., *et al*., 2022a. Modeling ultrasonic vibration fatigue with unified mechanics theory. International Journal of Solids and Structures. 236–237. https://doi.org/10.1016/j.ijsolstr.2021.111313. 111313.

Lee, H.W., Fakhri, H., Ranade, R., *et al*., 2022b. Modeling fatigue of pre-corroded body-centered cubic metals with unified mechanics theory. Materials & Design 224. 111383. https://doi.org/10.1016/j.matdes.2022.111383.

Lee, H.W., Djukic, M.B., Basaran, C., 2023. Modeling fatigue life and hydrogen embrittlement of bcc steel with unified mechanics theory. International Journal of Hydrogen Energy 48 (54), 20773–20803. https://doi.org/10.1016/j.ijhydene.2023.02.110.

Lemaitre, J., Sermage, J.P., Desmorat, R., 1999. A two scale damage concept applied to fatigue. International Journal of Fracture 97 (1/4), 67–81. https://doi.org/10.1023/a:1018641414428.

Li, X., Ma, X., Zhang, J., *et al*., 2020. Review of hydrogen embrittlement in metals: hydrogen diffusion, hydrogen characterization, hydrogen embrittlement mechanism and prevention. Acta Metallurgica Sinica (English Letters) 33 (6), 759–773. https://doi.org/10.1007/s40195-020-01039-7.

Liang, J.-W., 2005. Identifying Coulomb and viscous damping from free-vibration acceleration decrements. Journal of Sound and Vibration 282 (3–5), 1208–1220. https://doi.org/10.1016/j.jsv.2004.04.034.

Lim, C., (2014, January). lecture notes, butler-volmer equation I Electrochemical energy systems I Chemical engineering I MIT OpenCourseWare. MIT OpenCourseWare. https://ocw.mit.edu/courses/10-626-electrochemical-energy-systems1029 spring-2014/resources/mit10_626s14_s11lec13/

Lin, J., Liu, Y., Dean, T.A., 2005. A review on damage mechanisms, models and calibration methods under various deformation conditions. International Journal of Damage Mechanics 14 (4), 299–319. https://doi.org/10.1177/1056789505050357.

Lu, B.T., Luo, J.L., 2006. Synergism of electrochemical and mechanical factors in erosion – corrosion. The Journal of Physical Chemistry B 110 (9), 4217–4231. https://doi.org/10.1021/jp051985f.

Marion, J.B., 1965. Hamilton's principle—Lagrangian and Hamiltonian dynamics. In Classical Dynamics of Particles and Systems. Elsevier. pp. 214–266.

Marti, N., Favier, V., Gregori, F., Saintier, N., 2020a. Correlation of the low and high frequency fatigue responses of pure polycrystalline copper with mechanisms of slip band formation. Materials Science and Engineering: A 772. 138619. https://doi.org/10.1016/j.msea.2019.138619.

Marti, N., Favier, V., Gregori, F., Saintier, N., 2020b. Correlation of the low and high frequency fatigue responses of pure polycrystalline copper with mechanisms of slip band formation. Materials Science and Engineering: A 772. 138619. https://doi.org/10.1016/j.msea.2019.138619.

Martin, M.L., Dadfarnia, M., Nagao, A., Wang, S., Sofronis, P., 2019. Enumeration of the hydrogen-enhanced localized plasticity mechanism for hydrogen embrittlement in structural materials. Acta Materialia 165, 734–750. https://doi.org/10.1016/j.actamat.2018.12.014.

Mattsson, T.R., Mattsson, A.E., 2002. Calculating the vacancy formation energy in metals: Pt, Pd, and Mo. Physical Review B 66. 214110. https://doi.org/10.1103/PhysRevB.66.214110.

Mughrabi, H., 2009. Cyclic slip irreversibilities and the evolution of fatigue damage. Metallurgical and Materials Transactions B 40 (4), 431–453. https://doi.org/10.1007/s11663-009-9240-4.

Mughrabi, H., 2013. Cyclic slip irreversibility and fatigue life: A microstructure-based analysis. Acta Materialia 61 (4), 1197–1203. https://doi.org/10.1016/j.actamat.2012.10.029.

Naderi, M., Amiri, M., Khonsari, M.M., 2010. On the thermodynamic entropy of fatigue fracture. Proceedings of the Royal Society A: Mathematical, Physical and Engineering Sciences. 466423-438.

Nagao, A., Dadfarnia, M., Somerday, B.P., Sofronis, P., Ritchie, R.O., 2018. Hydrogen-enhanced-plasticity mediated decohesion for hydrogen-induced intergranular and 'quasi-cleavage' fracture of lath martensitic steels. Journal of the Mechanics and Physics of Solids 112, 403–430. https://doi.org/10.1016/j.jmps.2017.12.016.

Novak, P., Yuan, R., Somerday, B.P., Sofronis, P., Ritchie, R.O., 2010. A statistical, physical-based, micro-mechanical model of hydrogen-induced intergranular fracture in steel. Journal of the Mechanics and Physics of Solids 58 (2), 206–226. https://doi.org/10.1016/j.jmps.2009.10.005.

Novak, P.M., 2009. A dislocation-based constitutive model for hydrogen-deformation interactions and a study of hydrogen-induced intergranular fracture (Order No. 3406790). Available from ProQuest Dissertations & Theses Global. (288251968). Retrieved from https://www.proquest.com/dissertations-theses/dislocation-based-constitutive-model-hydrogen/docview/288251968/se-2?accountid=14169

Page, C.L., 2007. Corrosion and protection of reinforcing steel in concrete. Durability of Concrete and Cement Composites. 136–186. https://doi.org/10.1533/9781845693398.136.

Parvin, H., Kazeminezhad, M., 2016. Modelling the temperature rise effect through high-pressure torsion. Materials Science and Technology 32 (12), 1218–1222. https://doi.org/10.1080/02670836.2015.1114713.

Planck, M., 1900. Section 134: Entropie und Warscheinlichkeit. In Vorlesungen uber die theorie der wurmestrahlung. Germany: J.A. Barth: Leipzig. p. 1900.

Popov, B.N., 2015. Electrochemical kinetics of corrosion. Corrosion Engineering. 93–142. https://doi.org/10.1016/b978-0-444-62722-3.00003-3.

Popov, B.N., Lee, J.-W., Djukic, M.B., 2018. Hydrogen permeation and hydrogen-induced cracking. Handbook of Environmental Degradation of Materials. 133–162. https://doi.org/10.1016/b978-0-323-52472-8.00007-1.

Quinn, D.D., 2004. A new regularization of coulomb friction. Journal of Vibration and Acoustics 126 (3), 391–397. https://doi.org/10.1115/1.1760564.

Refait, P., Grolleau, A.-M., Jeannin, M., Rémazeilles, C., Sabot, R., 2020. Corrosion of carbon steel in marine environments: role of the corrosion product layer. Corrosion and Materials Degradation, [online] 1 (1), 198–218. https://doi.org/10.3390/cmd1010010.

Reza Abbaschian, Reed-Hill, R.E., Abbaschian, L., 2010. Physical Metallurgy Principles. Australia: Cengage Learning.

Roberts, M.H., 1954. A potentiostat for corrosion study. British Journal of Applied Physics 5 (10), 351–352. https://doi.org/10.1088/0508-3443/5/10/303.

Robertson, I.M., Sofronis, P., Nagao, A., *et al*., 2015. Hydrogen embrittlement understood. Metallurgical and Materials Transactions B 46 (3), 1085–1103. https://doi.org/10.1007/s11663-015-0325-y.

Shidong, Li, Abdulhamid, M.F., Basaran, C., 2009. Damage mechanics of low temperature electromigration and thermomigration. IEEE Transactions on Advanced Packaging 32 (2), 478–485. https://doi.org/10.1109/tadvp.2008.2005840.

Teng, Z., Wu, H., Boller, C., Starke, P., 2020. A unified fatigue life calculation based on intrinsic thermal dissipation and microplasticity evolution. International Journal of Fatigue 131. 105370. https://doi.org/10.1016/j.ijfatigue.2019.105370.

Torabian, N., Favier, V., Dirrenberger, J., *et al*., 2017. Correlation of the high and very high cycle fatigue response of ferrite based steels with strain rate-temperature conditions. Acta Materialia 134, 40–52. https://doi.org/10.1016/j.actamat.2017.05.064.

Voyiadjis, G.Z., Abed, F.H., 2005a. Microstructural based models for bcc and fcc metals with temperature and strain rate dependency. Mechanics of Materials 37 (2–3), 355–378. https://doi.org/10.1016/j.mechmat.2004.02.003.

Voyiadjis, George & Abed, Farid. (2005b). Effect of dislocation density evolution on the thermomechanical response of metals with different crystal structures at low and high strain rates and temperatures. Archives of Mechanics. 57.

Wasim, M., Djukic, M.B., 2020. Hydrogen embrittlement of low carbon structural steel at macro-, micro- and nano-levels. International Journal of Hydrogen Energy 45 (3), 2145–2156. https://doi.org/10.1016/j.ijhydene.2019.11.070.

Wasim, M., Djukic, M.B., Ngo, T.D., 2021. Influence of hydrogen-enhanced plasticity and decohesion mechanisms of hydrogen embrittlement on the fracture resistance of steel. Engineering Failure Analysis 123. 105312. https://doi.org/10.1016/j.engfailanal.2021.105312.

Yao, W., Basaran, C., 2013a. Electromigration damage mechanics of lead-free solder joints under pulsed DC: A computational model. Computational Materials Science 71, 76–88. https://doi.org/10.1016/j.commatsci.2013.01.016.

Yao, W., Basaran, C., 2013a. Computational damage mechanics of electromigration and thermomigration. Journal of Applied Physics 114 (10), 103708. https://doi.org/10.1063/1.4821015.

Yao, W., Basaran, C., 2013b. Damage mechanics of electromigration and thermomigration in lead-free solder alloys under alternating current: An experimental study. International Journal of Damage Mechanics 23 (2), 203–221. https://doi.org/10.1177/1056789513488396.

Zhang, H., Yan, L., Zhu, Y., *et al*., 2021. The effect of immersion corrosion time on electrochemical corrosion behavior and the corrosion mechanism of EH47 ship steel in seawater. Metals 11 (8), 1317. https://doi.org/10.3390/met11081317.